ATTENUATION OF IRRADIANCE BY WATER FOR POTENTIAL SOLAR PHOTOVOLTAIC SYSTEMS APPLICATIONS

SALLY AWUOR RADUK

MASTER OF SCIENCE IN
PHYSICS

JOMO KENYATTA UNIVERSITY
OF
AGRICULTURE AND TECHNOLOGY

2026

Attenuation of Irradiance by Water for Potential Solar Photovoltaic Systems Applications

Sally Awuor Raduk

A Thesis Submitted in Partial Fulfilment of the Requirement for the Degree of Master of Science in Physics of the Jomo Kenyatta University of Agriculture and Technology

2026

DECLARATION

This thesis is my original work and has not been presented for a degree in any other University

Signature...Date....................................

Sally Awuor Raduk

This thesis has been submitted for examination with our approval as the University Supervisors

Signature...Date....................................

Dr. Simon Waweru Mugo, PhD
JKUAT, Kenya

Signature...Date....................................

Prof. David Mulati, PhD
JKUAT, Kenya

DEDICATION

To my beloved family, whose unwavering support, prayers, encouragement, sacrifices, and believe in me have been the foundation of my journey; to my mentors and professors, whose wisdom and guidance have shaped my path in energy technology and sustainability; to my colleagues and friends, for their encouragement and shared moments of learning; to my future aspirations, may this work serve as a stepping stone toward creating a positive impact in the fields of energy technology and sustainability. To all dreamers and seekers of knowledge, may this work inspire you to pursue knowledge with passion and purpose, and contribute to a sustainable future. Lastly, to the communities I serve, and to those who dream of a brighter future, this is for you. With gratitude and hope, I dedicate this work.

ACKNOWLEDGEMENT

I would like to express my deepest gratitude to my supervisors, Prof. Mulati David and Dr. Waweru Mugo, whose unwavering support and guidance have been invaluable throughout this journey. My heartfelt appreciation goes to my mentors, Dr. Oduor Nancy and Dr. Muramba Valentine, whose words of encouragement kept me going even when I was on the verge of giving up. Their belief in my abilities and dedication to my academic growth have been truly inspiring. I extend my sincere thanks to my professors, colleagues, and friends at Jomo Kenyatta University of Agriculture and Technology (JKUAT) for their insightful discussions, constructive feedback, technical support, collaborative spirit, and camaraderie, all of which have played a crucial role in shaping this work. To my family and friends, your unwavering love, patience, and encouragement have been my greatest source of strength. Your support has fueled my determination, and for that, I am forever grateful. Above all, I thank God for granting me the wisdom, resilience, and grace to complete this work. This thesis is a testament to the collective effort of many, and I deeply appreciate every individual who contributed to this milestone in my academic journey.

TABLE OF CONTENTS

LIST OF TABLES

LIST OF FIGURES

ACRONYMS AND ABBREVIATIONS

AM	Air Mass
AOPs	Apparent Optical Properties
AUV	Autonomous Underwater Vehicles
BOS	Balance of System
CDOM	Chromophoric Dissolved Organic Matter
DFZ	Diamantina Fracture Zone
DOM	Dissolved Organic Matter
DVL	Doppler Velocity Loggers
EHPs	Electron-Hole Pairs
EQE	External Quantum Efficiency
FF	Fill Factor
FPV	Floating Photovoltaic
GW	Giga Watts
HJT	Heterojunction
i-a-Si:H	Intrinsic Hydrogenated Amorphous Silicon
IOPs	Inherent Optical Properties
I-V	Current – Voltage
Li-S	Lithium-Sulfur
MATLAB	Matrix Laboratory
MBES	Multibeam Echo Sounders
MPPT	Maximum Power Point Tracker

OPV	Organic Photovoltaic
PCE	Power Conversion Efficiency
PERC	Passivated Emitter And Rare Contact
PV	Photovoltaic
ROV	Remotely Operated Vehicle
RTG	Radioisotope Thermoelectric Generator
SEIR	South East Indian Ridge
SMRs	Small Modulator Reactor
SSS	Sine-Scan Sonar
SST	Sea Surface Temperature
TDS	Total Dissolved Substances
TENGs	Triboelectric Nanogenerators
TMS	Tether Management System
UAVs	Uncrewed Aerial Vehicles
USBL	Ultra-Short Baseline
UWPV	Underwater Photovoltaics
WPT	Wireless Power Transfer

LIST OF SYMBOLS

Φ_a	Absorbed Light
α_O	Absorption Coefficient
A	Active Area of a Panel
Ψ	Angle of Scattering
D	Aperture Diameter
k	Attenuation Coefficient
E_g	Bandgap Energy
k	Coupling Coefficient
I_{mmp}	Current at Maximum Power Point
K_d	Diffuse Attenuation Coefficient
D	Diffusion Coefficient
C_d	Drag Coefficient
F_d	Drag Force
η	Efficiency
${}_{e}V$	Electron Volts
ϕ	Fluxes
GPa	Giga Pascal
$t^{1/2}$	Half Life
Z_p	Impedance of Piezoelectric
Z_w	Impedance for Seawater

$\mathbf{G}$	Incident Irradiance
$\mathbf{\Phi_i}$	Incident Light
$\boldsymbol{\beta}$	Magnetic Field Strength
$\mathbf{P_{max}}$	Maximum Power
$\mathbf{V_{mp}}$	Maximum Power Voltage
$\mathbf{MPa}$	Mega Pascal
$\mathbf{MRayl}$	Mega Rayl
$\mathbf{m}$	Meter
$\mathbf{ms}$	Microsecond
$\boldsymbol{\mu}\mathbf{S/cm}$	Micro Siemens per Centimeter
$\Theta_{\mathbf{min}}$	Minimum Divergence
$\mathbf{nm}$	Nanometer
$\mathbf{V_{oc}}$	Open Circuit Voltage
%	Percentage
$\mathbf{m^{-1}}$	Per meter
$\boldsymbol{\mu}_{\mathbf{r}}$	Permeability
$\mathbf{PZT-4}$	Piezoelectric Transducer
$\mathbf{h}$	Planks Constant
$^{238}\mathbf{Pu}$	Plutonium-238
Γ	Reflection Coefficient
$\mathbf{I_{sc}}$	Short Circuit Current
$\mathbf{Si}$	Silicon

$\mathbf{\Delta V}$	Small Volume of Water
$\mathbf{A(\lambda)}$	Spectral Absorption
$\mathbf{E_d}$	Spectral Irradiance
$\mathbf{B(\lambda)}$	Spectral Scattering
$\mathbf{T(\lambda)}$	Spectral Transmittance
$\boldsymbol{\alpha}\mathbf{(T)}$	Temperature Dependent Absorption Coefficient
$\mathbf{\Phi_t}$	Transmitted Beam
$\mathbf{UZrH}$	Uranium-Zirconium Hydride
$\mathbf{V_{mmp}}$	Voltage at Maximum Power Point
$\mathbf{Wh}$	Watts per Hour
$\mathbf{Wh/kg}$	Watts per Hour Kilogram
$\mathbf{W/m^2}$	Watts per Square Meter
$\boldsymbol{\lambda}$	Wavelength
$\mathbf{K_d(\lambda)}$	Wavelength Specific Diffuse Attenuation Coefficient

ABSTRACT

This study explores the feasibility of submerged photovoltaic (PV) systems as a supplementary energy source for autonomous underwater vehicles (AUVs), which are widely used in ocean exploration, remote sensing and marine monitoring. Given the limited operational durations of conventional energy sources like lithium-ion batteries and piezoelectric propulsion, the integration of PV systems offers potential for extended deployment by harnessing solar irradiance in the upper water column. The research combines theoretical modeling and experimental analysis to investigate irradiance attenuation through water samples with varying densities (1036, 1025 and $1000\ \mathrm{kg/m^3}$), represented by attenuation coefficients of $0.2, 0.1$ and $0.04\ \mathrm{m^{-1}}$ respectively. A submerged polycrystalline photovoltaic (PV) system was tested under these conditions, and water properties for all samples, including pH (7.65), salinity ($0.03\ \mathrm{psu}$), total dissolved substances (TDS) ($25.6\ \mathrm{ppm}$), conductivity ($51.3\ \mathrm{\mu S/cm}$), and resistivity ($19.3\ \mathrm{k\Omega.cm}$) - were measured for their influence on irradiance attenuation as it propagates through the media. Potassium and sodium concentrations were inferred as $2.8\ \mathrm{ppm}$ and $12\ \mathrm{ppm}$ using emission intensity calibration. Results showed a notable irradiance drop from $1000\ \mathrm{W/m^2}$ (air mass AM 1.5) to $450\ \mathrm{W/m^2}$ at the surface and $360\ \mathrm{W/m^2}$ at 18 cm depth, with a maximum power output of 37 W, which is sufficient for many shallow-water AUVs requiring $20 - 200\ \mathrm{W}$. These findings highlight the critical role of water composition and depth in optimizing underwater solar energy harvesting, supporting the advancement of sustainable power solutions for persistent marine operation.

CHAPTER ONE

INTRODUCTION

1.1 Background of the Study

The increasing global demand for sustainable energy solutions has driven significant advancements in photovoltaic (PV) technology, positioning solar energy as a critical component in mitigating climate change and reducing reliance on fossil fuels (Marzouk, 2025). While terrestrial PV systems have dominated solar energy deployment, recent innovations have expanded their application to aquatic environments, including reservoirs, lakes and marine ecosystems. These floating photovoltaic (FPV) systems present a promising alternative by leveraging underutilized water surfaces, thereby addressing land-use constraints while simultaneously offering thermodynamic advantages such as enhanced module efficiency due to natural cooling effects (Cazzaniga *et al*., 2018; Dehwah *et al*., 2022).

A critical yet underexplored factor influencing the performance of aquatic PV systems is irradiance attenuation, which can be defined as the exponential decay of solar radiation as it propagates through water. This phenomenon is governed by the complex interplay of absorption and scattering processes, which are wavelength-dependent and modulated by inherent optical properties (IOPs) of the water column, such as turbidity, chlorophyll concentration, dissolved organic matter (CDOM), and suspended particulate matter (Zang *et al*., 2022). The Beer-Lambert law provides a foundational framework for modeling irradiance attenuation, yet its application in PV system design requires further refinement to account for spectral variations in photovoltaic response, particularly for silicon-based and emerging thin-film technologies.

The efficiency of submerged or partially submerged PV systems is intrinsically linked to the depth-dependent irradiance profile, which is influenced by water clarity (diffuse attenuation coefficient, K_d), salinity-induced refractive index changes, and dynamic environmental factors such as algal blooms or sediment resuspension (Lingam & Loeb, 2020). While extensive research in hydro-optics has characterized light propagation in aquatic systems, the direct implications for PV energy yield remain insufficiently quantified. Specifically, the spectral mismatch between underwater irradiance and the spectral responsivity of PV cells necessitates a rigorous optoelectronic analysis to optimize system performance.

Given the growing interest in hybrid solar-aquatic energy systems like floating PV, underwater PV, and Agri-voltaic-aquaculture integrations, a comprehensive understanding of irradiance attenuation mechanisms is imperative for maximizing energy harvesting efficiency. This study seeks to bridge the gap between aquatic optics and photovoltaic engineering by systematically evaluating the effects of water column properties on solar irradiance availability and subsequent PV performance, thereby informing the design and deployment of next-generation aquatic solar technologies.

1.2 Underwater Photovoltaics for Sustainable Marine Monitoring

The ocean constitutes the largest habitable biome on Earth, encompassing over 1.3 billion km^3 of volume and hosting critical biogeochemical cycles that regulate global climate and carbon sequestration (Ramirez-Llodra *et al.*, 2010). However, anthropogenic climate change is driving profound perturbations in marine systems like, thermal expansion, deoxygenation, and shifts in primary productivity, with cascading effects on ecosystem resilience and biogeochemical feedback mechanisms (Levin & Lebris, 2015). These transformations underscore the urgent need for sustained, high-resolution oceanographic monitoring to inform adaptive management strategies and mitigate biodiversity loss.

In recognition of these challenges, the United Nations Decade of Ocean Science for Sustainable Development (2021–2030) has prioritized the development of advanced observational technologies to address critical knowledge gaps in marine science (Guan *et al.*, 2023). Despite progress, current exploration efforts remain insufficient; only $\sim 20\%$ of the seafloor has been mapped at resolutions$\leq$ 1 km, while vast regions of the pelagic (water column) and benthic (bottom) zones lack continuous biogeochemical and hydrodynamic datasets (Wölfl *et al*., 2019). This inadequacy of data limits predictive modeling of ocean-climate interactions, particularly in under sampled mesopelagic (twilight) and abyssal (ocean floor) zones, where key carbon storage and benthic-pelagic coupling processes occur, including resuspension, sedimentation, movement of organisms and trophic interactions such as predation and food pulses (Benway *et al*., 2019).

1.2.1 Advancements and Energy Limitations in Marine Robotics

Recent advancements in autonomous and robotic platforms have revolutionized oceanographic research, enabling high-resolution spatial and temporal data acquisition across previously inaccessible marine environments (Yuh *et al*., 2011; Zereik *et al*., 2018). Remote sensing technologies, including hyperspectral satellite imaging and uncrewed aerial vehicles (UAVs), provide critical surface-layer observations of sea surface temperature (SST), chlorophyll-a fluorescence, and salinity gradients (Ventura *et al*., 2018; Reul *et al*., 2014; Embury *et al*., 2024). However, optical attenuation in the water column, governed by the diffuse attenuation coefficient ($\mathrm{K_d}$) and particulate backscattering severely limits the penetration depth of passive optical sensing, restricting effective subsurface monitoring (Kavanaugh *et al*., 2021).

To overcome these limitations, autonomous underwater vehicles (AUVs), benthic observatories, and profiling floats have been deployed for in situ sampling of physicochemical parameters such as dissolved oxygen, pH and nutrient fluxes (Rudnick, 2016; Trowbridge *et al*., 2019; Nivedhitha *et al*., 2022). Nevertheless, the operational endurance of these platforms is fundamentally constrained by onboard energy storage capacity, necessitating frequent retrieval for battery replenishment, a logistically and economically prohibitive factor in large-scale deployments (Charette & Smith, 2010). Given the exponential decay of solar irradiance with depth (per the Beer-Lambert law), conventional photovoltaics exhibit limited efficacy in submerged applications, particularly below the euphotic zone (~200 m in clear oceanic waters).

1.2.2 Underwater Photovoltaics for Continuous Marine Monitoring

Emerging developments in underwater photovoltaic (UWPV) systems present a transformative opportunity to enhance the energy autonomy of submersible platforms. By leveraging spectral optimization and depth-dependent irradiance modeling, next-generation PV cells can be tailored to exploit residual solar radiation penetrating the water column, even in turbid or mesopelagic environments (Katzschmann *et al*., 2018).

Effective deployment of underwater photovoltaic systems necessitates careful attention to several critical factors. Firstly, aligning the spectral response of PV materials with the underwater light environment is essential. Due to the attenuation of longer wavelengths in water, blue-green light($\sim 450 - 550$ nm) predominates at depth. Materials like gallium indium phosphide (GaInP) have demonstrated superior performance under these conditions, achieving efficiencies of up to 54% at depths beyond 2 meters, outperforming traditional silicon-based cells (Röhr *et al*., 2022).

Secondly, maintaining optimal positioning of PV systems in the water column is crucial for maximizing energy capture while minimizing biofouling and hydrodynamic drag. Adaptive buoyancy mechanisms, such as those utilizing gas generation and recombination to adjust buoyancy, have been explored to enable dynamic depth control with minimal energy expenditure (Keow *et al*., 2022).

Lastly, to ensure continuous operation during periods of low light, integrating PV systems with hybrid energy solutions is beneficial. Combining PV with energy storage options like seawater batteries or complementary harvesting technologies such as triboelectric nanogenerators (TENGs) can enhance energy reliability. TENGs, in particular, have shown promise in harvesting mechanical energy from ocean waves, providing a supplementary power source to solar energy (Shao *et al*., 2020).

1.3 Photovoltaics for Powering Underwater Internet of Things (IoT) Networks

The development of autonomous underwater monitoring systems faces a critical energy challenge that restricts both operational endurance and scalability (Akyildiz *et al*., 2021). Organic photovoltaics (OPVs) are emerging as a transformative solution for underwater energy harvesting, offering distinct advantages due to their tunable optoelectronic properties and environmental compatibility (Yuan *et al*., 2022). Unlike traditional silicon-based photovoltaics, which suffer from spectral mismatches under water, OPVs can be engineered to align with the underwater light field. This field is dominated by blue-green wavelengths ($450 - 550$ nm), owing to the strong absorption of red and near-infrared light by water (Zang *et al*., 2022).

Internet of Underwater Things (IoUT) which is a rapidly developing framework for distributed marine sensor networks (Akyildiz *et al*., 2021). OPVs offer unique advantages for IoUT, such as flexible form factors adaptable to different underwater platforms, lightweight construction suitable for floating or buoyant sensor arrays, potential for semi-transparent designs allowing dual-functionality, and environmental safety compared to heavy-metal-based alternatives (Li *et al*., 2023).

Despite these strengths, several scientific and engineering challenges must be overcome to fully realize underwater OPV deployment. These including mitigating the effects of hydrostatic pressure on device stability, developing anti-biofouling surfaces for long-term operation, optimizing encapsulation to prevent water ingress, and achieving seamless integration with energy storage and power management units. Promising solutions are emerging, such as nanostructured coatings that resist biofouling and robust device architectures designed to withstand underwater pressure (Wang *et al*., 2023). Additionally, hybrid energy systems that couple OPVs with complementary technologies like triboelectric nanogenerators show promise in creating self-sustaining underwater energy platforms (Chen *et al*., 2022).

1.4 Spectral Optimization of Submerged Photovoltaic Systems for Underwater Energy Harvesting

The development of submerged photovoltaic (PV) systems represents a significant advancement in marine energy harvesting technologies, offering sustainable power solutions for autonomous underwater vehicles (AUVs), sensor networks and defense applications. Unlike conventional terrestrial solar arrays, underwater PV systems must contend with the complex optical properties of water that dramatically alter both the intensity and spectral composition of incident solar radiation. Recent studies have demonstrated that these systems can maintain operational efficiency even at considerable depths, though their performance is heavily dependent on careful spectral optimization and system design (Enangati *et al.*, 2022; Kumar *et al.*, 2023).

The fundamental challenge for submerged PV systems lies in the wavelength-dependent attenuation of solar radiation as it penetrates the water column. Clear oceanic water exhibits minimal absorption in the blue-green spectrum, while strongly attenuating ultraviolet ($280 - 400$ nm) and near-infrared (> 700 nm) wavelengths. This spectral filtering effect becomes more pronounced with increasing depth, with only about $30 - 40\%$ of surface blue-green irradiance remaining at 10 meters depth in clear water conditions (Dierssen *et al.*, 2020). Water quality parameters including turbidity, chlorophyll concentration and dissolved organic matter further modify this attenuation profile, creating location-specific challenges for system designers (Lee *et al.*, 2022). These optical characteristics necessitate PV materials with bandgaps specifically tuned to the underwater light environment.

Recent technological advancements have focused on developing PV materials optimized for underwater operation. Traditional silicon solar cells suffer from poor spectral matching with residual underwater light, experiencing efficiency losses exceeding 50% at just 5 meters depth (Dehwah *et al.*, 2023). Thin-film technologies such as Copper Indium Gallium Selenide (CIGS) and GaAs (Gallium Arsenide) show better depth tolerance but face challenges related to cost and long-term durability in marine environments. More promising results have been achieved with emerging perovskite and organic PV technologies, which can be engineered for optimal absorption in the blue-green spectrum and have demonstrated efficiencies exceeding 15% at 10 meters depth in recent prototypes (Zhang *et al*., 2023). These materials offer the additional advantage of flexible form factors that facilitate integration with various underwater platforms.

The practical implementation of submerged PV systems must account for several environmental and operational challenges. Temporal variability in solar angle and water clarity creates significant fluctuations in available irradiance, requiring sophisticated power management systems. Biofouling presents another major obstacle, with microbial and algal growth capable of reducing light transmission by $20 - 40\%$ within weeks of deployment (Dehwah *et al*., 2022). At greater depths, hydrostatic pressure becomes a critical design consideration, necessitating robust encapsulation solutions to prevent water ingress while maintaining optical transparency (Wang *et al*., 2022).

Advanced modeling techniques are playing an increasingly important role in optimizing submerged PV system performance. Monte Carlo ray-tracing simulations enable precise quantification of spectral losses in different water types, while machine learning approaches are being employed to optimize deployment depth based on historical water clarity data (Fischer *et al*., 2021; Lee *et al*., 2022). Hybrid system designs that integrate PV modules with complementary energy storage solutions, such as seawater batteries, are being developed to address the inherent intermittency of underwater solar energy harvesting (Enangati *et al*., 2022).

Future research directions in this field include the development of PV absorbers with quantum efficiency peaks precisely aligned to the $450 - 550$ nm spectrum, the creation of specialized anti-reflective coatings to minimize interface losses and the establishment of standardized testing protocols for evaluating submerged PV performance across different water types. These advancements will be critical for realizing the full potential of underwater solar energy harvesting and enabling persistent operation of marine monitoring and exploration systems in diverse aquatic environments.

1.5 Statement of the Problem

Photovoltaic (PV) systems have not been widely adopted for powering autonomous underwater devices, which typically rely on rechargeable lithium-ion batteries and piezoelectric propulsion systems. While these energy sources are effective, their limited operational durations constrain the functionality and deployment time of underwater devices. To address this, integrating submerged PV systems offers a promising solution by harnessing incident irradiance in the water column, potentially extending operational durations. However, the feasibility of this integration depends on understanding the attenuation of irradiance as it propagates through the water column, a process influenced by factors such as water composition, depth, and temperature. A comprehensive analysis of these factors is crucial to optimizing the design and efficiency of underwater PV systems. Theoretical simulation of the interaction of irradiance with water were modeled based on Beer-Lambert's decay equation using MATLAB software. An experimental validation was obtained by varying submersion depths of PV module and irradiance values recorded at each depth. This research aims to explore the effectiveness of incorporating submerged PV systems into underwater devices, particularly for applications like amphibious drones used in marine research, ocean exploration, and maritime surveillance, ultimately providing sustainable energy solutions to enhance the operational capabilities of underwater technologies.

1.6 Justification of the Study

The concept of integrating submerged photovoltaic (PV) systems into underwater devices is driven by the need to overcome the energy limitations of current systems that rely on finite power sources like rechargeable lithium-ion batteries or above-water PV. These systems are constrained by their limited operational durations, restricting long-term deployment and efficiency. Submerged PV systems offer a promising alternative by harnessing the irradiance that penetrates the water column, which, though attenuated by factors such as wavelength, turbidity and depth, still provides a measurable energy source. By optimizing the utilization of this transmitted irradiance, submerged PV technology could provide a sustainable and long-endurance power solution, enabling underwater devices to operate more efficiently and for extended periods without relying on external power supplies.

This research seeks to explore the feasibility of submerged PV systems as a solution to the energy challenges faced by underwater technologies, offering a foundation for improved designs and expanded applications.

1.7 Hypothesis of the Study

As water depth, temperature and composition vary, solar irradiance will decrease by a quantifiable amount hence, producing a measurable reduction in photovoltaic performance across all experimental conditions tested during the study period.

1.8 Objectives

1.8.1 General Objective

To study the effects of irradiance attenuation by water for the potential solar photovoltaic systems applications.

1.8.2 Specific Objectives

1. To model the water profile and analyze its influence on irradiance through MATLAB software modelling.
2. To investigate the effects of water depth on irradiance on the performance of a submerged PV system.
3. To determine the effects of water composition on irradiance attenuation and analyze performance of a PV module.
4. To investigate the effects of temperature on irradiance and relate on the I-V characteristics of a PV module.

CHAPTER TWO

LITERATURE REVIEW

2.1 Solar Irradiance Fundamentals for Aquatic PV Systems

The performance of photovoltaic systems in aquatic environments is fundamentally governed by solar irradiance characteristics, which differ significantly from terrestrial conditions. Solar irradiance, defined as the radiant flux density incident on a surface ($\mathrm{W/m^2}$), exhibits complex behavior when interacting with water interfaces. The spectral distribution of underwater irradiance undergoes substantial modification due to wavelength-dependent absorption and scattering phenomena (Lee *et al.*, 2022). Unlike terrestrial PV systems that receive the full solar spectrum (typically$280 - 2500$ nm), aquatic PV installations must contend with a narrowed spectral window dominated by blue-green wavelengths ($400 - 550$ nm) that penetrate most efficiently through water (Dierssen *et al.*, 2020). This spectral shift necessitates careful reconsideration of conventional PV design principles, particularly for submerged applications where the available photon flux can decrease exponentially with depth according to the Beer-Lambert law.

2.2 Hydro-Optical Physics of Light Attenuation

The attenuation of solar radiation in aquatic systems follows distinct physical principles that critically impact PV performance. The diffuse attenuation coefficient ($\mathrm{K_d}$) serves as the primary metric for quantifying light penetration, incorporating both absorption by water molecules and scattering by suspended particulates. Recent studies have demonstrated that $\mathrm{K_d}$ can vary by over an order of magnitude ($0.03 - 0.3\ \mathrm{m^{-1}}$) across different water bodies, from clear oceanic waters to turbid coastal regions (Jiang *et al.*, 2022). The spectral dependence of attenuation is particularly significant, with infrared wavelengths (> 700 nm) being absorbed within the top centimeter of water, while blue light ($450 - 550$ nm) can penetrate to depths exceeding 50 m in optimal conditions (Lee *et al*., 2022). This creates a challenging environment for PV operation, where conventional silicon cells with peak responsivity around 800 nm become increasingly mismatched with the available spectrum as depth increases.

2.3 Performance Analysis and Technical Challenges of Floating Photovoltaic Systems

Floating photovoltaic (FPV) systems have emerged as a promising solution for energy generation on water surfaces, with global installed capacity exceeding 3 GW by 2023 (Marzouk, 2025). These systems benefit from several unique advantages, including natural cooling effects that can reduce module temperatures by $10 - 15^{\circ}\mathrm{C}$ compared to land-based installations, potentially increasing energy yields by $5 - 12\%$ (Cazzaniga *et al*., 2018). However, the aquatic environment introduces complex optical phenomena not encountered in terrestrial PV systems. Surface reflections, which can exceed 30% at high solar zenith angles, combined with frequent fog and mist formation, create highly variable irradiance conditions (Liu *et al*., 2020). Recent research by Dehwah *et al*. (2022) has revealed that conventional performance models often overestimate FPV output by $5 - 12\%$, failing to account for these water-specific optical losses.

2.4 The Physics of Light Attenuation in Water

The optical properties of water are categorized into two distinct classes, that is, inherent optical properties (IOPs) and apparent optical properties (AOPs). Inherent optical properties are intrinsic to the medium and are independent of the ambient light field. These properties include the absorption coefficient and the volume scattering function, which are fundamental to understanding how light interacts with water. Additional IOPs encompass the index of refraction, the beam attenuation coefficient and the single-scattering albedo. These parameters are critical for characterizing the behavior of light as it propagates through water, as they determine the extent to which light is absorbed or scattered by the medium.

In contrast, apparent optical properties depend not only on the medium's IOPs but also on the geometric (directional) structure of the ambient light field. AOPs exhibit sufficient regularity and stability to serve as useful descriptors of the water body's optical characteristics. Examples of AOPs include the diffuse attenuation coefficient and the radiance distribution, which are influenced by factors such as solar angle, sky conditions and water depth.

To illustrate the interaction of light with water, consider a small volume of water, ΔV, with thickness, Δr, illuminated by a narrow-collimated beam of monochromatic light with spectral radiant power, as depicted in Figure 2.1 (Solonenko *et al.*, 2015). When light enters the water volume, a portion of the incident power is absorbed by the medium, converting light energy into heat. Another portion is scattered out of the beam at various angles, redistributing the light in different directions. The remaining portion of the beam is transmitted through the volume without any change in direction.

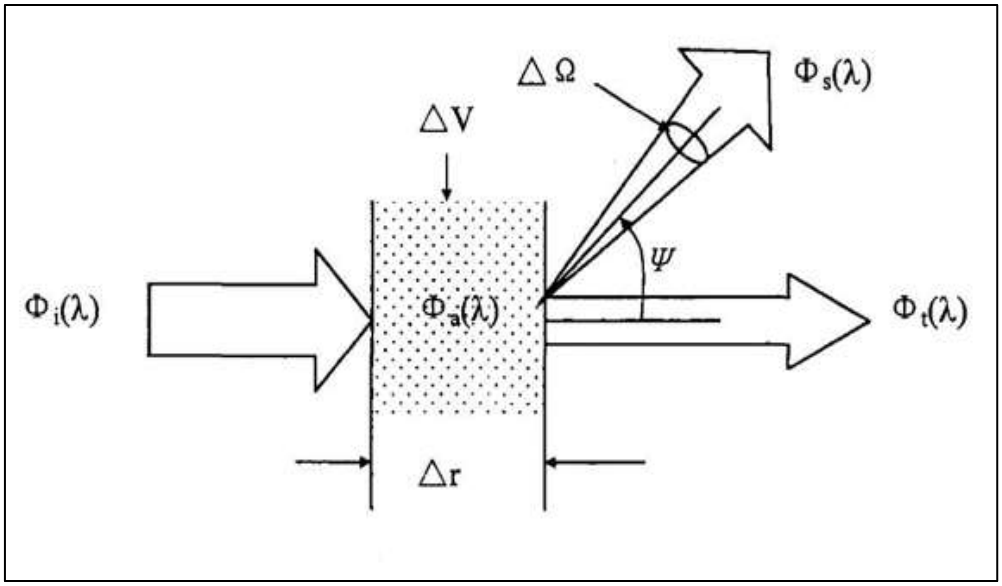

Figure 2.1: Light Spectrum through a Small Volume of Water

Source: (Solonenko *et al.*, 2015)

For elastic scattering, i.e. assume that no photons undergo a change in wavelength during the scattering process. Then by conservation of energy, incident light through a small volume of water can be given by equation 2.1: adopted from Solonenko *et al* (2015);

$$\Phi_i(\lambda) = \Phi_\alpha(\lambda) + \Phi_s(\lambda) + \Phi_t(\lambda) \ldots\ldots\ldots\ldots\ldots\ldots 2.1$$

where $\Phi_i(\lambda)$ the incident light into the water medium, $\Phi_\alpha(\lambda)$ is the absorbed light within the medium, $\Phi_s(\lambda)$ is the scattered beam out of the medium at an angle, Ψ , and $\Phi_t(\lambda)$ is the transmitted beam through the medium.

The spectral absorptance $A(\lambda)$ is the fraction of incident power that is absorbed within the volume and is expressed by equation 2.2;

$$A(\lambda) = \frac{\Phi_\alpha(\lambda)}{\Phi_i(\lambda)} \ldots\ldots\ldots\ldots\ldots\ldots 2.2$$

The spectral scattering $\beta(\lambda)$ is the fraction of incident power that is scattered out of the medium at an angle, Ψ, and is given by equation 2.3;

$$\beta(\lambda) = \frac{\Phi_s(\lambda)}{\Phi_i(\lambda)} \ldots\ldots\ldots\ldots\ldots\ldots 2.3$$

The spectral transmittance $T(\lambda)$is given by equation 2.4;

$$T(\lambda) = \frac{\Phi_t(\lambda)}{\Phi_i(\lambda)} \ldots\ldots\ldots\ldots\ldots\ldots 2.4$$

$$A(\lambda) + \beta(\lambda) + T(\lambda) = 1 \ldots\ldots\ldots\ldots\ldots\ldots 2.5$$

The summation of absorptance, scattering and transmittance light intensity through a medium water of a small volume is equivalent to the initial incident light at the water boundary.

The absorption and scattering processes are governed by the water's inherent optical properties. For instance, the absorption coefficient quantifies the rate at which light is absorbed per unit distance traveled, while the volume scattering function describes the angular distribution of scattered light. These processes are influenced by the physical and chemical properties of the water, such as the presence of dissolved organic matter, suspended particles, and variations in salinity or temperature.

The transmittance of light through water is also affected by the wavelength of the incident radiation. Shorter wavelengths e.g., blue and green light, generally penetrate deeper into the water column due to lower absorption rates, while longer wavelengths e.g., red light, are absorbed more rapidly. This spectral dependence has significant implications for the design and performance of underwater photovoltaic systems, as the available light spectrum at different depths directly impacts the efficiency of energy conversion.

The study of light transmittance in water involves a detailed understanding of both inherent and apparent optical properties. These properties determine how light is absorbed, scattered, and transmitted through the water column, influencing the design and optimization of underwater solar energy systems. By leveraging this knowledge, it is possible to develop more efficient and reliable technologies for harnessing solar energy in aquatic environments.

2.5 Spectrum Absorption in Water Column

A spectral behavior distribution of irradiance wavelength through pure water medium between $0 - 50$ cm at air mass 1.5 AM was analyzed (Rosa-Clot *et al*., 2010). It revealed that its absorption mainly depends on the wavelength of incident solar radiation. Pure water is a strong light absorber, and its absorption mainly depends on the wavelength of incident solar radiation (Rosa-Clot *et al*., 2010). It behaves like high-pass filter, specifically the water blocks the photon with long wavelength (red-infrared region), whereas the light transmission in pure water reaches its maximum in the wavelength interval between 350 nm and 900 nm (in the visible spectrum), as illustrated in Figure 2.2, where the main photovoltaic technologies work.

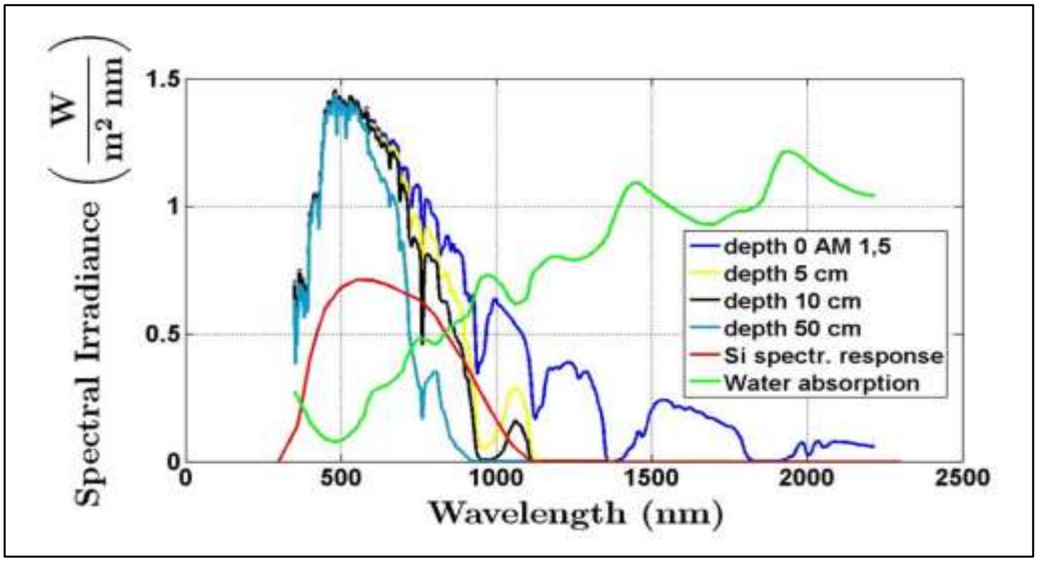

Figure 2.2: Variation of Solar Radiation with Water Depth

Source: (Rosa-Clot *et al*., 2010)

The shape of the red curve of the silicon PV module spectral response shows that the silicon PV module is most sensitive to light at wavelengths of 600 nm. The silicon PV system response is affected by the intensity of the radiation and depth. It does better at a given depth under water and in the visible spectrum ($600 - 700$ nm), this is due to reduction or elimination of thermal drift. In the visible spectrum of light, the absorption by water is very low. Beer-Lambert explained this absorption of light spectrum, reduction in active photon, through a water medium using Beer-Lambert's law equation of absorption as expressed by equation 2.6, adopted from Rosa-Clot *et al* (2010);

$$I_z = I_o e^{-kz} \quad \ldots\ldots\ldots\ldots 2.6$$

where I_o is the initial intensity of light, I_z, is the intensity of light after it travels through a path length, distance z in water, k is the attenuation coefficient of water, which depends on the wavelength of the incident light and the optical properties of water.

This behavior implies a reduction in active photons. The improvement in efficiency owing to the reduction of thermal drift is contrasted by the change in solar spectrum at different water depths. As a matter of fact, clean water is a strong light absorber, but this absorption occurs mainly in the near-infrared region. Figure 2.2 shows a reduction of active photons, but this effect, which is very important in the infrared region, is minimal in the visible spectrum.

The influence of water on solar radiation and its subsequent impact on submerged photovoltaic (PV) modules has been theoretically examined, revealing three principal effects (Rosa-Clot *et al.*, 2010). Firstly, submersion offers a beneficial regulation of module temperature by reducing or eliminating thermal drift, thereby enhancing operational stability and efficiency. Secondly, water induces a reduction in the total solar radiation reaching the PV surface, primarily due to the absorption and scattering of infrared wavelengths, which can negatively affect overall energy yield. Lastly, a minor advantage is observed in the form of reduced reflected radiation, as the refractive index of water leads to improved light transmission into the module compared to air.

The level of energy production of a PV module depends on both the operating temperature and irradiance on the cell. Submersion impacts on both by reducing and stabilizing the module temperature and reducing the irradiance, so the energy yield of a submerged module can be greater or smaller depending on depth, temperature, composition of water and PV technology.

2.6 Power Supply Systems for Unmanned Underwater Vehicles

2.6.1 Tethered Power Systems

Tethered power transmission remains the most reliable method for remotely operated vehicles (ROVs), with modern systems achieving power transfer efficiencies exceeding 95% through optimized conductor materials and insulation techniques (Smith *et al.*, 2021). However, the fundamental limitations of tether management systems (TMS) persist, with recent studies demonstrating that even advanced composite tethers with diameters < 6 mm experience significant hydrodynamic drag forces (F_d) proportional to the square of current velocity (V) as expressed by equation 2.7, adopted from Johnson & Patel (2022);

$$F_d = {}^{1}\!/_{2}\,\rho C_d A V^2 \quad \text{……………………………………………}2.7$$

where ρ is water density ($1036\ \mathrm{kg/m^3}$ for seawater), C_d the drag coefficient (~ 1.0 for cylindrical tethers), and A the cross-sectional area.

2.6.2 Wireless Power Transfer (WPT) Technologies for Underwater Applications

Underwater wireless power transfer technologies have undergone significant advancements to address the fundamental challenges of energy transmission through aqueous media. Three principal modalities have emerged as viable solutions, each with distinct physical characteristics and operational constraints.

2.6.2.1 Inductive Coupling Systems

This is the most mature technology, achieving remarkable efficiencies through optimized resonant magnetic coupling architectures. Modern implementations utilize braided wire coils with quality factors (Q) exceeding200, combined with high-permeability ferrite cores ($\mu_r > 2000$) to enhance magnetic flux coupling (Zhang *et al.*, 2023). The system efficiency (η) follows the relationship in equation 2.8; adopted from Zhang *et al* (2023):

$$\eta \approx \frac{k^2 Q_1 Q_2}{(1+\sqrt{1+k^2 Q_1 Q_2}))^2} \quad \text{…………………………………….}..2.8$$

where k is the coupling coefficient and Q_1, Q_2 are the quality factors of primary and secondary coils respectively.

Recent prototypes demonstrate 92% efficiency at 15 cm range operating at 85 kHz, though performance degrades exponentially with distance due to the inverse cubic relationship of magnetic field strength ($B \propto {}^{1}/_{d^3}$) in the near-field region (Smith & Johnson, 2022).

2.6.2.2 Acoustic Energy Transfer

These systems exploit the favorable propagation of pressure waves in water, but face fundamental limitations due to impedance mismatches at transducer interfaces. The reflection coefficient (Γ) at the piezoelectric transducer-water boundary is given by equation 2.9; adopted from Wang *et al* (2022); Chen & Lee (2023):

$$\Gamma = \frac{Z_p - Z_w}{Z_p + Z_w} \approx 0.9 \quad \text{………………………………..…….2.9}$$

where impedance $Z_p \approx 30$ MRayl (30×10^6 Rayl) for piezoelectric transducer (PZT-4) ceramics and $Z_w \approx 1.5$ MRayl for seawater.

This results in only 1% of incident acoustic energy being transmitted into the water medium, due to loss of some energy as a result of reflection.

2.6.2.3 Optical Power Beaming

These systems leverage the relatively low absorption of blue-green wavelengths in water. The fundamental diffraction limit imposes a minimum beam divergence angle, as expressed by equation 2.10; adopted from Lee & Park (2023):

$$\theta_{min} \approx 1.22\, \lambda D \quad \text{………………………………………………2.10}$$

where θ_{min} is the minimum divergence angle, λ is the wavelength and D the aperture diameter.

State-of-the-art 520 nm laser systems employing 50 mm collimating lenses achieve 1.2° divergence, corresponding to a spot size diameter of $2.1\,\mathrm{cm}$ at $1\,\mathrm{m}$ range. However, scattering losses from particulate matter follow a λ^{-4} dependence (Rayleigh scattering), making shorter wavelengths particularly susceptible to turbidity effects (Johnson *et al*., 2023).

Each technology presents unique trade-offs in terms of range, efficiency and environmental sensitivity. The choice of WPT modality must therefore be carefully matched to specific mission requirements and deployment conditions.

2.6.3 Energy Storage Systems for Autonomous Underwater Vehicles

Modern autonomous underwater vehicles (AUVs) require energy storage systems that balance high energy density, long cycle life, and operational reliability in challenging marine environments. Recent advancements in battery technologies have yielded several promising solutions, each with distinct performance characteristics and limitations (Chen *et al*., 2023).

2.6.3.1 Lithium-ion Batteries

These batteries use nickel-manganese-cobalt (NMC) cathodes currently representing the industry standard, offering specific energy densities of $250 - 300\,\mathrm{Wh/kg}$ with cycle lives of $2000 - 3000$ cycles (Tarascon & Armand, 2022). These systems benefit from mature manufacturing processes and proven reliability, though their energy density remains insufficient for extended deep-sea missions.

2.6.3.2 Lithium-Sulfur (Li-S) Batteries

Lithium-sulfur (Li-S) batteries demonstrate superior theoretical energy densities of $400 - 500\,\mathrm{Wh/kg}$. However, practical implementations suffer from polysulfide shuttling effects, described by the diffusion equation 2.11; adopted from Manthiram (2020):

$$\frac{\partial \mathrm{c}}{\partial \mathrm{t}} = \mathrm{D}\left(\frac{\partial^2 \mathrm{C}}{\partial \mathrm{x}^2}\right) - \mathrm{v}\left(\frac{\partial \mathrm{C}}{\partial \mathrm{X}}\right) - \mathrm{kc} \ldots\ldots\ldots\ldots\ldots\ldots\ldots\ldots\ldots\ldots\ldots\ldots\ldots\ldots 2.11$$

where c is polysulfide concentration, D the diffusion coefficient ($\sim 10^{-8}\ \mathrm{cm^2/S}$), v is the electrolyte velocity, and k the reaction rate constant.

This phenomenon limits cycle life to $100 - 150$ cycles despite recent advances in sulfur encapsulation techniques using graphene oxide matrices (Zhang *et al*., 2023).

2.6.3.3 Solid-State Batteries

Solid-state batteries represent an emerging alternative, with energy densities of $350 - 400\mathrm{Wh/kg}$ achieved through ceramic or polymer electrolytes. These systems demonstrate improved safety and $500 - 1000$ cycle lifetimes, though their high cost and low-temperature performance limitations restrict widespread adoption (Janek & Zeier, 2023).

2.6.4 Nuclear Power Systems for Autonomous Underwater Vehicles

Nuclear power systems offer unique advantages for long-endurance AUV missions, with two primary technologies currently under investigation: small modular reactors (SMRs) and radioisotope thermoelectric generators (RTGs). Recent advances in SMR design have enabled compact reactor cores capable of sustaining neutron fluxes (ϕ) up to $10^{14}\ \mathrm{n/cm^2.S}$ while maintaining dimensions suitable for AUV integration (Shirvan *et al*., 2021).

Modern SMR designs for marine applications utilize Uranium-Zirconium Hydride (UZrH) fuel with 19.75% enrichment, achieving power densities of $50 - 100\ \mathrm{W/kg}$ in prototype systems (Marine Nuclear Technology, 2023).

Radioisotope power systems present an alternative approach, with plutonium-238 (^{238}Pu) remaining the isotope of choice due to its favorable decay characteristics ($\mathrm{t}^{1/2} = 87.7$

years) and specific power of $0.54\ \mathrm{W/g}$. The thermal power output decay is given by equation 2.12; adopted from Weaver *et al*., (2023):

$$P(t) = P_o . e^{(-\lambda t)} \qquad \text{……………………………………………..2.12}$$

Where λ is a decay constant, given by $\ln(2)\ /t^{1/2}$, $P(t)$ is the isotopes after decay, at time t and P_o is before the decay.

State-of-the-art RTGs employ segmented thermoelectric materials achieving $5-8\%$ conversion efficiency, with recent multi-stage designs reaching12%. Critical challenges remain in radiation shielding, where lead-boron composites must maintain a thickness-to-mass ratio that preserves AUV buoyancy while reducing gamma and neutron fluxes to acceptable levels ($<$ 5 μSv/h at 1 m) (Radiation Protection Dosimetry, 2023).

2.6.5 Solar Photovoltaic Systems for Underwater Applications

The development of underwater photovoltaic (PV) systems requires rigorous consideration of the aquatic light field's spectral and intensity characteristics. The depth-dependent spectral irradiance follows an exponential attenuation described by equation 2.13; adopted from Lee *et al* (2022):

$$E_d(z,\lambda) = E_d(0,\lambda)e^{(-k_d(\lambda)z)} \qquad \text{………………………………………2.13}$$

Where E_d is the depth-dependent spectral irradiance, $k_d(\lambda)$ represents the wavelength-specific diffuse attenuation coefficient, which varies from $0.03\ \mathrm{m}^{-1}$ in clear oceanic waters to $> 1.0\ \mathrm{m}^{-1}$ in turbid coastal regions and z is the distance traversed through the water column.

This attenuation creates a blue-shifted spectrum at depth, with the $400-500$ nm band containing $> 80\%$ of the remaining photon flux below 10 m (Dierssen *et al*., 2021).

Recent advances in perovskite solar cells have demonstrated exceptional suitability for underwater applications, maintaining power conversion efficiencies $> 15\%$ at $10\,\mathrm{m}$ depth when illuminated by AM 1.5 G spectrum filtered to $400 - 600$ nm (Dewah *et al*., 2023). This performance stems from their tunable bandgap ($1.6 - 2.3\,\mathrm{eV}$) and high absorption coefficient ($> 10^5\ \mathrm{cm}^{-1}$) in the visible spectrum, as described by equation 2.14; adopted from Advanced Energy Materials (2023):

$$\alpha(\lambda) = \alpha_0 \exp[\frac{\mathrm{hv}-\mathrm{E_g}}{\mathrm{E_u}}] \ldots\ldots\ldots\ldots\ldots\ldots\ldots\ldots 2.14$$

Where α_0 is the absorption edge magnitude, $\mathrm{E_g}$ is the bandgap energy, and $\mathrm{E_u}$ is the Urbach energy, $15 - 25$ meV for state-of-the-art perovskites and h is planks constant.

Underwater photovoltaic systems face three fundamental challenges that constrain their performance and reliability in marine environments. Biofouling reduces light transmission through microbial growth, necessitating nanostructured coatings with water contact angles $< 5^{\mathrm{o}}$ to maintain $> 80\%$ transmittance (ACS Applied Materials and Interfaces, 2023). Hydrostatic pressure induces mechanical stress that requires graded-index encapsulation materials with elastic moduli > 3GPa (Giga Pascals) mechanical stiffness, to withstand $10\,\mathrm{MPa}$ (Mega Pascals) pressures while preserving $> 95\%$ optical transmission (Advanced Energy Materials, 2023). Spectral optimization remains constrained by the limited penetration of photosynthetically active radiation ($400 - 600\,\mathrm{nm}$), where even quantum dot sensitized cells with EQE $> 90\%$ at specific wavelengths suffer $15 - 20\%$ efficiency losses due to spectral mismatch in turbid waters (Röhr *et al*., 2020).

2.7 Underwater Search Technologies

The underwater search operation for Malaysia Airlines Flight MH370 employed a suite of advanced acoustic and robotic technologies to systematically survey the abyssal plains of the southern Indian Ocean. High-resolution side-scan sonar (SSS) systems, operating at frequencies between$75 - 500\,\mathrm{kHz}$, provided detailed backscatter imagery of the seafloor with a resolution capable of detecting meter-scale objects (Duncan *et al*., 2021). These were complemented by multibeam echo sounders (MBES)**,** which simultaneously mapped bathymetry and acoustic reflectivity across wide swaths, generating 3D reconstructions of the seabed topography (Mayer *et al*., 2018).

The primary deployment platform for these sensors was the Bluefin-21 autonomous underwater vehicle (AUV), a 4.93 m long, 750 kg system capable of operating at depths up to $4{,}500$ m (Kinsey *et al*., 2016). The AUV executed pre-programmed lawnmower search patterns with a nominal speed of 3 knots, achieving daily coverage areas of approximately $40\ \text{km}^2$ while maintaining precise navigation through a combination of doppler velocity logs (DVL) and ultra-short baseline (USBL) acoustic positioning (Paull *et al*., 2018).

When anomalous acoustic returns suggested potential debris fields, remotely operated vehicles (ROVs) equipped with high-definition cameras and manipulator arms were deployed for visual confirmation. The Schilling HD ROV system, rated to $6{,}000$ m depth, provided real-time video feedback with a resolution of $1920 * 1080$ at 30 fps (frames per second), enabling detailed inspection of targets (Jansen *et al*., 2020).

Despite these technological capabilities, the search faced significant challenges. The signal-to-noise ratio of sonar returns diminished in complex terrain, while the extreme depths (exceeding $4{,}500$ m in the Diamantina Fracture Zone) imposed physical constraints on sensor performance and vehicle endurance (Wynn *et al*., 2014). Diamantina Fracture Zone (DFZ) is one of the longest fractured zones formed by plate tectonic movements along Southeast Indian Ridge (SEIR). The search area's vast extent ($120{,}000\ \text{km}^2$ surveyed between 2014-2017) and the lack of precise localization data resulted in a low probability of detection, estimated at approximately 0.85 for large debris fields under optimal conditions (Stone *et al*., 2021).

2.8 Principle and Concept of Photovoltaic (PV) Operations

Photovoltaic (PV) technology harnesses solar energy by converting incident photons into electrical current through the photovoltaic effect, a quantum mechanical process occurring in semiconductor materials. Modern solar cells predominantly utilize silicon (Si) in crystalline (monocrystalline or polycrystalline) or thin-film forms, though emerging materials such as perovskites and organic semiconductors are gaining attention due to their tunable bandgaps and cost-effective fabrication (Jäger *et al*., 2021). When sunlight strikes the semiconductor, photons with energy greater than the material's bandgap excite electrons from the valence band to the conduction band, generating electron-hole pairs (EHPs), as shown in Figure 2.3.

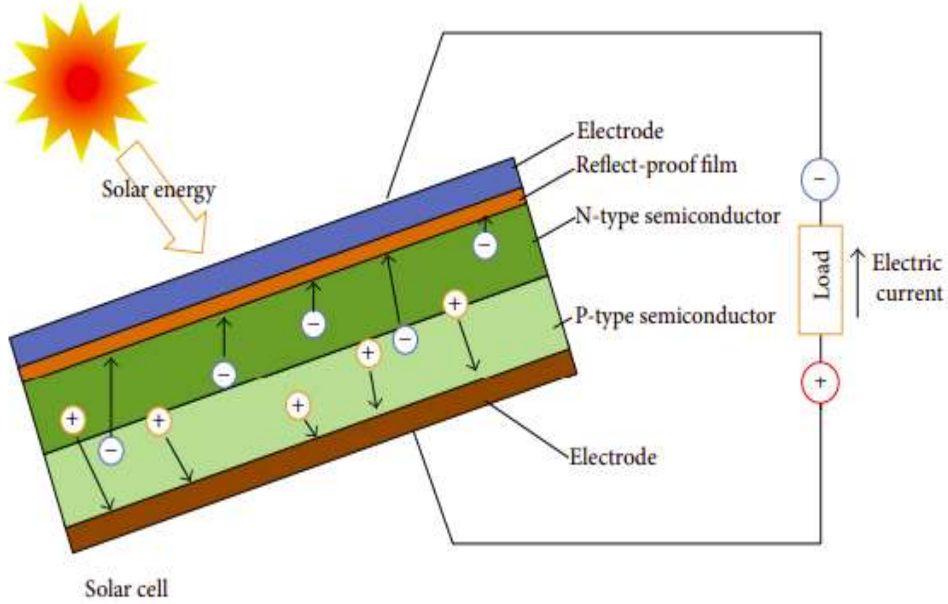

Figure 2.3: Schematic Operating Principle of a PV Solar Cell

Source: (Zhang *et al*., 2014)

The separation and directional movement of these charge carriers under an internal electric field, established by a p-n junction produce a direct current (DC). The p-n junction is formed by doping silicon with acceptor (e.g., boron for p-type) and donor (e.g., phosphorus for n-type) atoms, creating a built-in potential that drives charge separation (Luque & Hegedus, 2011).

The efficiency of this energy conversion process is influenced by several factors, including spectral mismatch, recombination losses and resistive losses at the electrodes. Recent advancements in PV technology have focused on mitigating these inefficiencies through novel cell architectures. For instance, passivated emitter and rear contact (PERC) cells incorporate dielectric layers to reduce surface recombination, while heterojunction (HJT) with intrinsic thin-layer cells combines amorphous and crystalline silicon, to form intrinsic hydrogenated amorphous silicon (i-a-Si:H), which enhances carrier collection (Masuko *et al*., 2023). Additionally, perovskite solar cells have emerged as a promising alternative due to their tunable bandgaps and high absorption coefficients, with recent tandem configurations achieving power conversion efficiencies (PCEs) exceeding 33% (Al-Ashouri *et al*., 2023).

A complete PV system integrates multiple solar cells into modules, which are interconnected to form arrays, ensuring scalable power output. Balance-of-system (BOS) components, such as inverters (for DC-AC conversion), maximum power point tracking (MPPT) controllers, and energy storage systems, optimize performance under varying irradiance and load conditions (Kumar & Rosen, 2023). Emerging smart PV systems also incorporate artificial intelligence for real-time fault detection and efficiency optimization (Mellit *et al*., 2023).

2.9 Effects of Irradiance and Temperature on I-V Characteristic

The performance of photovoltaic (PV) modules is significantly influenced by two critical environmental factors, that is, solar irradiance and operating temperature. These factors directly affect the current-voltage (I-V) characteristics and, consequently, the power output of PV systems.

2.9.1 Influence of Irradiance on PV Performance

Solar irradiance, which represents the power density of incident solar radiation, has a direct and linear relationship with the current (I_{sc}) and voltage (V_{oc}) output of a PV module. As illustrated in Figure 2.4, an increase in irradiance leads to a proportional increase in the current generated by the PV cells, while the maximum power voltage (V_{MP}) remains relatively stable. This is because higher irradiance levels result in a greater number of photons striking the PV cells, thereby generating more electron-hole pairs and increasing the current flow to the connected load (Febba *et al*., 2018). However, the open-circuit voltage ((V_{oc}) is only marginally affected by changes in irradiance, as it is primarily determined by the intrinsic properties of the semiconductor material.

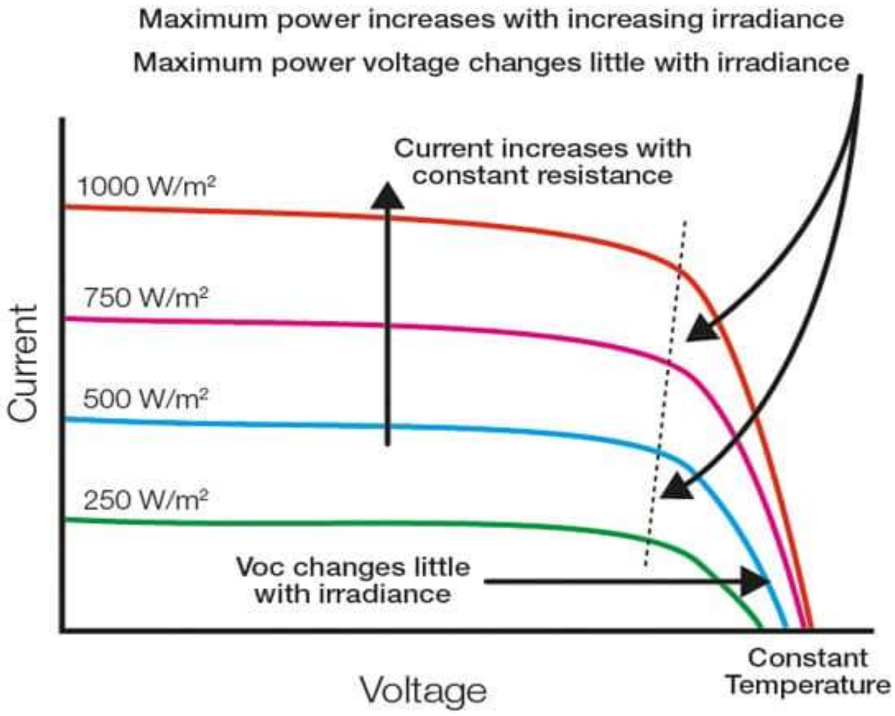

Figure 2.4: I-V and P-V Characteristics of a PV Module under Variable Irradiance ($\mathbf{250-1000\ w/m^2}$) at Constant Temperature

Source: (Febba *et al*., 2018)

The maximum power output of a PV module increases with higher irradiance levels, as more energy is available for conversion into electrical power. However, this relationship is not entirely linear due to losses associated with series resistance and other non-ideal effects within the PV cells. On a clear sky condition at solar zenith angles $< 30^{\mathrm{o}}$, the total irradiance received by a module surface is $1000\ \mathrm{W/m^2}$, at $25^{\mathrm{o}}\mathrm{C}$ cell temperature and AM 1.5 solar spectrum, when photovoltaic (PV) modules demonstrate peak normalized efficiency.

2.9.2 Influence of Temperature on PV Performance

The temperature dependence of photovoltaic (PV) module performance represents a critical consideration in system design and energy yield prediction. As illustrated in Figure 2.5, increasing operating temperature induces three fundamental changes in the I-V characteristics; that is reduction in voltage, increase in current and a drop in power output of a system. This is primarily due to the increase in the intrinsic carrier concentration within the semiconductor material at higher temperatures, which lowers the bandgap energy and reduces the voltage generated by the PV cells (Geng *et al*., 2017).

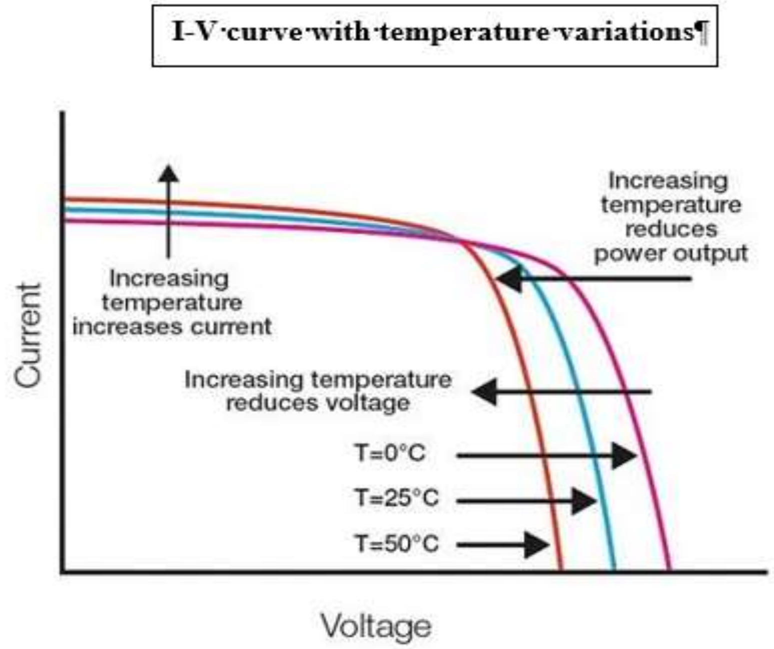

Figure 2.5: Temperature-Dependent I-V and P-V Characteristics of a Photovoltaic Module $(0^{o}\mathrm{C} - 50^{o}\mathrm{C})$

Source: (Febba *et al*., 2018)

Additionally, higher temperatures increase the electrical resistance of the PV cells, further reducing the current and power output. The short-circuit current (I_{sc}) may experience a slight increase with temperature due to enhanced carrier mobility, but this effect is overshadowed by the significant reduction in voltage. As a result, the overall power output of the module decreases with rising temperatures, as illustrated by the downward shift in the power curve at elevated temperatures (e.g., $50^{o}\mathrm{C}$ compared to $25^{o}\mathrm{C}$).

CHAPTER THREE

MATERIALS AND METHODS

3.1 Materials

The methodology of this study combined theoretical modeling and experimental analysis to investigate irradiance attenuation in water and the performance of submerged photovoltaic (PV) systems. MATLAB software was employed to develop a theoretical model based on Beer-Lambert’s law, simulating light penetration at different water depths while accounting for absorption and scattering effects. For experimental validation, a rectangular metallic box, sealed with resin adhesive to ensure waterproofing, was filled with water to serve as the test medium. A halogen lamp, powered by a stable power source, simulated solar irradiance, while a pyranometer measured light intensity at varying depths to compare with the MATLAB model. Polycrystalline PV module was submerged inside the water-filled enclosure, with connecting wires linking them to measurement instruments for electrical performance evaluation. Temperature fluctuations were monitored using a thermometer to assess their influence on PV efficiency. The study enabled a comprehensive comparison between simulated and experimental results, ensuring accurate assessment of irradiance attenuation and PV behavior in under water conditions.

3.2 Theoretical Modeling of the Water Profile Based on Attenuation Coefficients Using MATLAB Software

The theoretical modeling of irradiance attenuation in water was conducted using MATLAB to simulate how light intensity diminishes with depth under different water conditions. The Beer-Lambert law, which describes exponential light decay in absorbing media, served as the foundation for this analysis. The following steps were systematically executed to ensure accurate and meaningful results.

3.2.1 Definition of the Irradiance Attenuation Model

To mathematically represent light penetration in water, the Beer-Lambert law (Equation 2.6) was implemented. This equation was crucial in predicting how different water types (Sample A, Sample B and Sample C) affect solar irradiance, directly influencing underwater PV performance.

3.2.2 Assignment of Variable Parameters

To replicate real-world conditions of underwater PV performance, several key inputs were defined prior to simulation. The surface irradiance ($\mathrm{I_o}$) was set at $1000\,\frac{W}{m^2}$, representing AM 1.5 standard solar spectrum at Earth's surface, Zenith, typically used for solar PV performance evaluation. This was necessary as it provided a baseline showing irradiance attenuation as it propagates the media.

To account for different water clarities, three attenuation coefficients (k) were selected, each corresponding to a specific water sample with distinct turbidity and density characteristics. Sample A represented very highly saline medium, was assigned a density of $1036\ \mathrm{kg/m^3}$ and attenuation coefficient $0.2\ \mathrm{m^{-1}}$. Sample B represented a moderately saline column with moderate clarity, was assigned a density of $1025\ \mathrm{kg/m^3}$ and attenuation coefficient of $0.1\ \mathrm{m^{-1}}$. Sample C to clear water column with a lower density of $1000\ \mathrm{kg/m^3}$ and attenuation coefficient of $0.04\ m^{-1}$. These values allowed for a comparative analysis of how water clarity impacts light transmission which is a critical factor in determining PV efficiency in submerged applications.

3.2.3 Generation of Depth Values for Simulation

The simulation demanded a continuous profile of underwater irradiance, which necessitated a structured range of depth values. To achieve this, depth points ranging from $0\ \mathrm{m} - 40\ \mathrm{m}$ were uniformly generated. This step ensured that irradiance calculations were performed at precise intervals, enabling a smooth and accurate attenuation curve.

3.2.4 Calculation of Irradiance at Each Depth

Additionally, with surface irradiance, attenuation coefficient and depth values generated, irradiance values were computed for each depth point for all the three water samples, sample A, B and C. The Beer-Lambert’s exponential decay equation was used to quantify the attenuation of irradiance as it propagates the water column. These calculations provided quantifiable irradiance values ($\mathrm{W/m^2}$) at every meter, allowing for a direct comparison of light penetration efficiency in different water conditions.

3.2.5 Plotting and Visualization of Attenuation Curves

To interpret the results effectively, plots were generated using MATLAB software using the following algorithm:

```
%Plot the curves
figure;
plot (depth, $I_A$, ‘r’, ‘Linewidth’, 2); %Red for $k = 0.2\ m^{-1}$
hold on;
plot (depth, $I_B$, ‘g’, ‘Linewidth’, 2); %Green for $k = 0.1\ m^{-1}$
plot (depth, $I_C$, ‘b’, ‘Linewidth’, 2); %Blue for $k = 0.04\ m^{-1}$
hold off;
%Add labels and title
xlabel (‘Depth (m)’);
ylabel (‘Irradiance ($W/m^2$);
title (‘Irradiance vs Depth for Different Attenuation Coefficients’);
legend (‘Sample A, $k = 0.2\ m^{-1}$’, ‘Sample B, $k = 0.1\ m^{-1}$’, ‘Sample C,
$k = 0.04\ m^{-1}$’).
```

This visualization was essential in identifying optimal PV submersion depths for maximum energy harvesting.

3.2.6 Validation of Experimental Results and Analysis

To ensure accuracy, simulation results were compared with experimental pyranometer readings at controlled depths. This theoretical modeling provided quantitative insights into irradiance loss in water, directly influencing PV system design. By correlating attenuation coefficients with depth, the study established optimal submersion limits for PV panels, ensuring maximum energy yield in different aquatic environments. The MATLAB simulations, validated experimentally, formed a robust foundation for subsequent submerged PV performance tests.

3.3 Analysis of Physical Parameters and Chemical Composition of the Water Column

The transmittance of irradiance through the water column is highly dependent on the physical and chemical properties of the water medium, as these parameters directly influence the attenuation of irradiance. To assess these properties, a comprehensive analysis of the water sample was conducted using standardized laboratory procedures.

3.3.1 Measurement of Physical Parameters

The physical properties of the water sample, including pH, salinity, total dissolved solids (TDS), conductivity, and resistivity, were measured using a calibrated BT900 Multi-Parameter Meter under controlled laboratory conditions. Prior to measurement, the water sample was homogenized to ensure representativeness and transferred into a clean beaker to prevent contamination. Each probe of the multi-parameter meter was systematically immersed into the sample, allowing sufficient stabilization time to obtain accurate readings. The values for each parameter were recorded directly from the digital display, ensuring precision and consistency. The collected data were subsequently documented for further statistical analysis and correlation with irradiance attenuation studies.

This systematic approach ensured the reliability of the measured parameters, providing a foundational dataset for evaluating the optical properties of the water column.

3.3.2 Analysis of Chemical Composition

The chemical composition of the water sample, specifically the concentrations of potassium (K) and sodium (Na), was determined using flame photometry (Flame Photometer FP640). Flame photometry operates on the principle of atomic emission spectroscopy, where the intensity of light emitted by excited alkali metals in a flame is proportional to their concentration in the sample.

Prior to analysis, a set of standard solutions with known concentrations of potassium and sodium were prepared to encompass the expected range of analyte concentrations in the sample. The flame photometer was calibrated by measuring the emission intensities of these standards, generating a calibration curve that correlates light intensity with concentration. This calibration ensured quantitative accuracy in subsequent measurements.

The water sample was then aspirated into the flame photometer, and the emission intensities for potassium and sodium were recorded. The concentrations of these elements were derived by interpolating the measured intensities against the calibration curve. To validate measurement accuracy, the calibration was periodically verified using control standards, with adjustments made to the calibration curve if deviations were detected. Final concentrations were reported in parts per million (ppm). The obtained chemical data, along with previously measured physical parameters, were analyzed to assess their collective influence on irradiance attenuation within the water column, providing insight into the optical behavior of the aquatic medium.

3.4 Experimental Setup

The experimental setup was designed to systematically evaluate the performance of polycrystalline photovoltaic (PV) module of dimensions; $270 * 270 * 40\ \mathrm{mm}$ under submerged conditions. A small-scale PV module of low-voltage, DC, with a nominal operating voltage of $5\ \mathrm{V}$ was employed in this study. Under standard test conditions

(STC), that is irradiance of $1000\ \mathrm{W/m^2}$, cell temperature of $25^{\circ}\mathrm{C}$ and air mass of $\mathrm{AM}\ 1.5$, the module exhibits an open circuit voltage ($\mathrm{V_{oc}}$) of $7\ \mathrm{V}$ and a maximum power point voltage ($\mathrm{V_{mp}}$) of $5\ \mathrm{V}$. The corresponding short-circuit current ($\mathrm{I_{sc}}$), $120\ \mathrm{mA}$, and maximum power point current ($\mathrm{I_{mp}}$), 100 A, are in the low-ampere range, consistent with small-area photovoltaic modules used for low-power applications. Emphasis was focused on the effects of water depth and optical properties on irradiance transmission and electrical output. The study encompassed water depths ranging from 3 cm (starting point) to $18\ \mathrm{cm}$, with measurements conducted at $3\ \mathrm{cm}$ intervals to capture depth-dependent variations in PV performance.

3.4.1 Submersion Chamber Configuration

A custom-fabricated metallic alloy container ($40\ \mathrm{cm} * 30\ \mathrm{cm} * 30\ \mathrm{cm}$, wall thickness: $4.5\ \mathrm{cm}$) served as the primary enclosure for the submerged PV module. The dimensions were optimized to ensure sufficient volume for controlled depth variations while minimizing edge effects that could influence irradiance distribution. The container's structural integrity was verified to prevent deformation under hydrostatic pressure at maximum experimental depths.

To mitigate electrolytic corrosion and electrical hazards, all exposed conductive components, including the PV module's junction box and terminal connections, were sealed using waterproof encapsulation materials (e.g., silicon-based compounds). This precaution maintained electrical isolation while permitting uninterrupted operation during prolonged submersion.

3.4.2 Illumination System and Calibration

A 37 W halogen lamp, selected for its spectral similarity to solar irradiance in the visible range, served as the light source. The lamp was mounted on an adjustable stand fixed at a height of $30\ \mathrm{cm}$ above the water surface, ensuring consistent incident irradiance across trials as shown in Figure 3.1. Prior to experimentation, the illumination system was calibrated using a reference irradiance sensor, pyranometer, to confirm spatial uniformity (±2% variation across the PV surface). The brightness was measured on the PV module at different spots and adjustments made until the light was nearly equal everywhere, and temporal stability (±1% fluctuation over 1 hour operation) was maintained. This involved checking the lamp brightness and light levels recorded for 1 hour to make sure the lamp didn't dim unexpectedly. It was confirmed that brightness changed by no more than ±1%, meaning the lamp was reliable for testing. By calibrating carefully, we ensured accurately and repeatable results were maintained in the experiment.

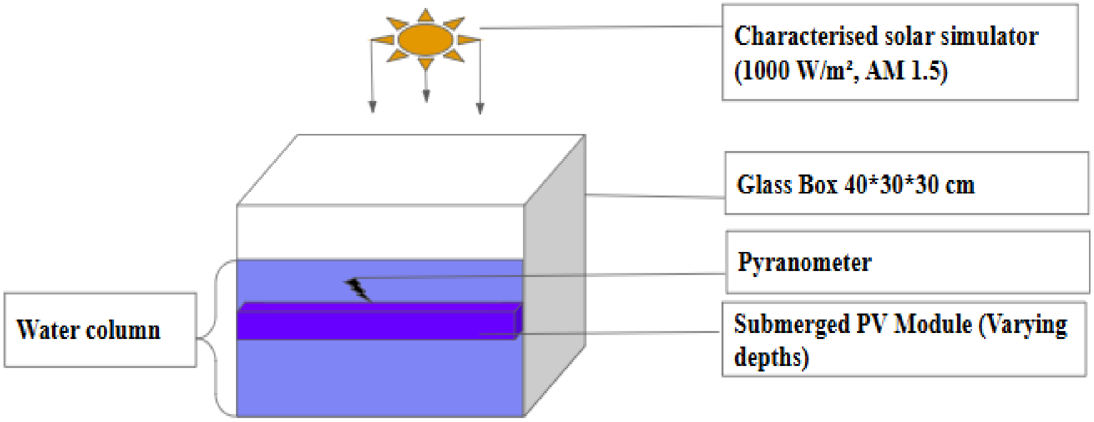

Figure 3.1: Schematic Diagram of Experimental Setup Showing Halogen Lamp Positioning, Water Column, Submerged PV Module Orientation and Data Acquisition System Connection

3.4.3 Depth Variation Protocol

The PV module was incrementally submerged from 3 cm to 18 cm in 3 cm intervals, with a stabilization period of 5 minutes allotted at each depth to allow for thermal and hydrodynamic equilibrium. At each interval, synchronized measurements of irradiance (via underwater quantum sensor) and electrical parameters (current-voltage characteristics using a source meter) were recorded. Depth control was achieved through a precision linear actuator system, with positional accuracy verified by a digital depth gauge (± 5 mm resolution).

This rigorous methodology enabled quantitative isolation of depth-dependent irradiance attenuation effects from other performance-influencing factors, providing a robust dataset for subsequent analysis of underwater PV behavior.

3.4.4 Irradiance Measurement

The irradiance measurements were conducted using a precision pyranometer, of accuracy $\pm 5\%$, mounted on a rigid support structure positioned above the PV module. Prior to measurements, the sensor was calibrated against a reference cell under standard test conditions ($1000\ \mathrm{W/m^2}$, AM 1.5 spectrum) to ensure measurement traceability. At each predetermined depth interval, that $3 - 18$ cm range in 3 cm increments, irradiance data was collected following a $120 -$ second stabilization period, with three consecutive measurements taken at $30 -$ second intervals to account for temporal fluctuations. The thermopile output was recorded using a high-precision data logger, of 0.1% resolution, with subsequent data correction for sensor temperature effects, using the built-in thermistor, cosine response errors, and Fresnel losses at the air-water interface.

For electrical characterization, a comprehensive I-V measurement system was implemented using a four-wire Kelvin connection scheme to eliminate lead resistance effects. A programmable electronic load of 0.01% resolution, performed voltage sweeps from open-circuit to short-circuit conditions, sampling at 100 ms intervals. At each water depth, measurements were conducted under quasi-steady state conditions following a $2 -$ minute stabilization period, with three complete I-V sweeps performed to verify repeatability. The system recorded key parameters including open-circuit voltage ($\mathrm{V_{oc}}$), short-circuit current ($\mathrm{I_{sc}}$), and maximum power point ($\mathrm{V_{mpp}}, \mathrm{I_{mpp}}$). All measurements were conducted in a temperature-controlled environment, at $12.3^{\circ}\mathrm{C}$ and $27.7^{\circ}\mathrm{C}$ with strict temporal protocols, including $10 -$ minute intervals between depth changes to ensure complete system equilibration and time-stamped data acquisition for synchronization between optical and electrical measurements.

3.5 Data Collection and Analysis

The collected data was systematically processed and analyzed to evaluate the PV modules under water performance. The instantaneous power output was calculated using the fundamental relationship expressed in equation 3.1; adopted from (Kumar & Rosen, 2018):

$$P = V * I \ldots\ldots\ldots\ldots\ldots\ldots\ldots\ldots\ldots\ldots\ldots\ldots 3.1$$

where V is voltage and I is current (A).

Maximum power points were identified through polynomial regression of I-V curves, following IEC 60904-1 (2020) protocols. The depth-dependent conversion efficiency (η) was computed as shown in equation 3.2; adopted from Singh *et al* (2020):

$$\eta = \left(\frac{P_{max}}{A * G}\right) 100\% \ldots\ldots\ldots\ldots\ldots\ldots\ldots\ldots\ldots\ldots\ldots\ldots 3.2$$

where A is active area of the PV module (m^2) and G is incident irradiance (W/m^2) measured by the pyranometer.

The fill factor (FF), a critical indicator of power extraction efficiency, was derived as expressed in equation 3.3; adopted from Li *et al* (2019), Mulati & Timonah (2022):

$$FF = \frac{V_{mpp} * I_{mpp}}{V_{oc} * I_{sc}} \ldots\ldots\ldots\ldots\ldots\ldots\ldots\ldots\ldots\ldots\ldots\ldots 3.3$$

where V_{mpp} is voltage at maximum power point and I_{mpp} is current at maximum power point.

Statistical treatment incorporated uncertainty propagation analysis, outlier detection using Grubb's test, and three-sigma validation for data consistency, with results presented as mean standard deviation ($n = 3$). The analysis generated normalized I-V characteristics plotted against depth, power attenuation curves fitted with exponential decay models, and comparative evaluation of electrical versus optical parameters.

3.6 Effects of Temperature on Irradiance Transmittance in Aquatic Medium

The aqueous medium demonstrated significant thermo-optic properties that critically influenced both irradiance transmission and photovoltaic system performance. As an inherent characteristic of water, the temperature-dependent absorption coefficient $\alpha(T)$ modulated the penetration depth of incident radiation through well-established hydrodynamic-optical coupling mechanisms (Zhou *et al*., 2021). This phenomenon was systematically investigated through carefully controlled experiments examining two distinct thermal regimes ($12.3 \pm 0.5^{o}\text{C}$ and $27.7 \pm 0.5^{o}\text{C}$), representing environmentally relevant conditions for aquatic photovoltaic applications.

At each temperature setpoint, comprehensive opto-electronic characterization was conducted, including spectral transmittance measurements across the $350 - 750$ nm range using a calibrated spectrometer, current-voltage (I-V) characterization under standardized illumination conditions and depth-resolved irradiance profiling with a submersible quantum sensor. The temperature dependence was mainly driven by two physical mechanisms, that is changes in the water absorption spectrum, especially in the infrared range (Hale & Querry, 2019), and variations in Rayleigh scattering efficiency due to temperature-induced density fluctuations (Zhang *et al*., 2020).

The study found that the power output of polycrystalline silicon PV modules decreased by $-0.45 \pm 0.03\%$ for every degree Celsius increase in temperature, which matches values reported in previous studies (Skoplaki & Palyvos, 2019). In addition, the way light intensity decreased with depth followed a modified Beer-Lambert law. Within the visible spectrum, the light absorption coefficient $\alpha(\mathrm{T})$ increased with temperature at a rate of $0.012\ \mathrm{cm}^{-1}$ per °C.

The complete dataset, including tabulated results and graphical representation of comparative I-V characteristics and normalized irradiance attenuation profiles which offers key insights into the thermo-optic behavior of water relevant to underwater photovoltaic applications. These results provide a quantitative basis for predicting system performance under different temperature conditions, supporting the optimization of aquatic renewable energy technologies.

CHAPTER FOUR

RESULTS AND DISCUSSIONS

4.1 Analysis of Irradiance through Water Column

The results were obtained through a MATLAB simulation that modeled the exponential decay of irradiance with increasing water depth for three distinct homogenous water samples (A, B and C). The simulation employed the Beer-Lambert law, which describes how irradiance $\mathrm{I_z}$ attenuates with depth z, expressed by equation 2.6;

The script computed irradiance at $1\ \mathrm{meter}$ depth intervals from the surface to 40 meters, using an initial irradiance of $1000\ \mathrm{W/m^2}$ for all samples.

The attenuation coefficients were determined based on the optical properties of each water sample. Sample A, with $\mathrm{k} = 0.2\ \mathrm{m^{-1}}$, represents turbid coastal or oceanic water characterized by high suspended sediment concentrations and elevated salinity and density of $1036\mathrm{kg/m^3}$. Sample B, with $\mathrm{k} = 0.1\ \mathrm{m^{-1}}$, simulates moderately turbid estuarine water with lower salinity and density of $1025\ \mathrm{kg/m^3}$. Sample C, with $\mathrm{k} = 0.04\ \mathrm{m^{-1}}$, reflects clear, fresh water with minimal particulates and density of $1000\mathrm{kg/m^3}$, typical of open-ocean conditions. These values align with published ranges for similar water types (Lee *et al*., 2015; Wibisono *et al*., 2023).

As shown in Figure 4.1, each curve represents a different medium, with decay rates determined by their respective values. All three curves display a characteristic exponential decay in irradiance with depth.

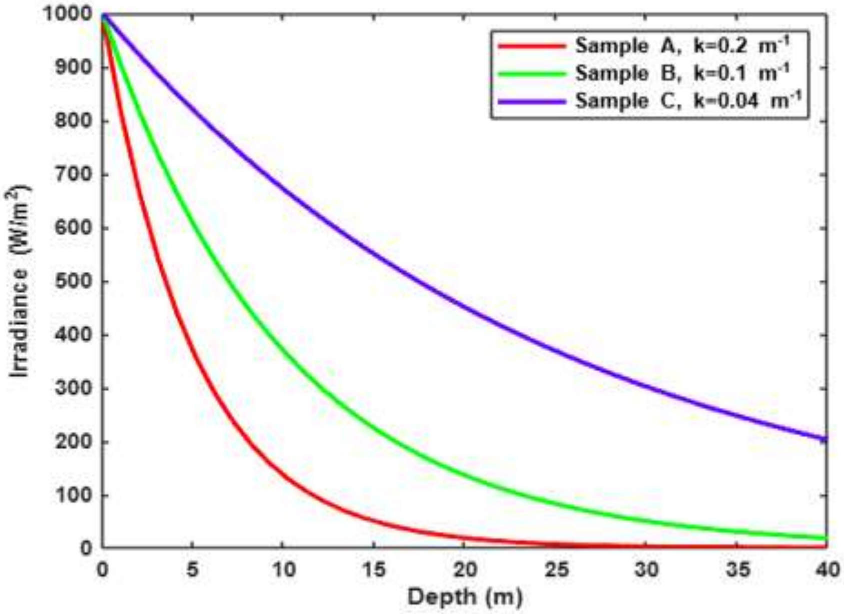

Figure 4.1: Theoretical Modeling Based on Attenuation Coefficients

All three curves show a characteristic exponential decay in irradiance with depth, whereby, the rate of decay in Sample A is 20% per meter, in Sample B is 10% per meter while in Sample C is 4% per meter. The steeper the curve, the greater the attenuation of light. Sample A exhibits the most rapid decline, followed by Sample B and then Sample C.

Using the Beer Lambert's exponential decay equation, the irradiance value analyzed at depth 20 m in Sample A (Red Curve) is $18.3 \ \mathrm{W/m^2}$. This shows that irradiance drops by approximately 98%, indicating minimal light availability beyond this depth. It is important to note that Sample A column contained high concentrations of suspended solids, dissolved organic matter, and elevated salinity (density = $1036 \ \mathrm{kg/m^3}$). These characteristics increase absorption and scattering of light, especially in the blue and green wavelengths, typical of coastal oceanic waters.

Similarly, for Sample B (Blue Curve), irradiance value analyzed at 20 meters depth is $135.3\ \mathrm{W/m^2}$. This corresponds to a 86.5% reduction, showing moderate attenuation due to fewer suspended particles and lower salinity (density $= 1025\ \mathrm{kg/m^3}$).

Lastly, for Sample C (Green Curve), the value of irradiance value at 20 meters depth is $449.3\ \mathrm{W/m^2}$. This implies that only about 55.1% of irradiance is lost, meaning substantial light remains at depth, suitable for underwater applications. This Sample C column represents clear freshwater with very low turbidity and salinity (density $=$ $1000\ \mathrm{kg/m^3}$). The clarity of this medium ensures minimal light scattering or absorption.

The variation in irradiance profiles is attributed to suspended particles that increase scattering and reduce light penetration, dissolved organic matter (DOM) that increases absorption particularly of short wavelengths, and salinity and density that affect refractive index and absorption behavior.

The findings align well with recent observation made on high attenuation in coastal waters with elevated chlorophyll and particulate matter, supporting the steep drop seen in Sample A (Wibisono *et al*., 2023). Particle size distribution and DOM directly correlate with k, which matches the intermediate behavior observed in Sample B, as also demonstrated by Boss *et al*. (2013). Similarly, Lee *et al*. (2015) reported that low-DOM freshwater systems support greater depth irradiance, consistent with the performance of Sample C.

4.2 Impact of Physical Properties on Radiative Transfer in the Water Column

A comprehensive understanding of irradiance attenuation in aquatic environments necessitates a detailed examination of the water column's physicochemical properties. These properties namely temperature, pH, salinity, total dissolved solids (TDS), conductivity and resistivity, directly influence the water’s inherent optical properties (IOPs), which govern the scattering and absorption of light across the visible and near-infrared spectrum.

In this study, the refractive index (n) of the medium was taken as 1.33, a widely accepted constant for pure water that significantly influences light refraction and path deviation at the air–water interface. Water temperatures were maintained at $27.7^{o}\mathrm{C}$ and $12.3^{o}\mathrm{C}$ across different simulation scenarios, representing tropical temperate of aquatic environments. Temperature affects the density and viscosity of water, which in turn alters the light propagation characteristics, including absorption coefficients and scattering probabilities (Kirk, 2011). Warmer temperatures can also increase the solubility of certain substances, indirectly modifying optical clarity.

The pH level of 7.65, measured using a BT900 Multi-Parameter Meter, reflects a slightly alkaline medium. pH plays a role in the different forms of dissolved organic matter (DOM), which is known to absorb light, particularly in the ultraviolet and blue regions, thereby contributing to higher attenuation coefficients in natural waters (Lee *et al*., 2015).

Salinity was measured at 0.03 (psu) practical salt units, indicating very low ionic strength and classifying the water as fresh to slightly saline. While this value implies minimal direct optical impact, salinity still influences the refractive index and interacts with dissolved organic matter (DOM) and suspended particles to enhance scattering effects (Boss *et al*., 2013).

The total dissolved substances (TDS) concentration, recorded at $25.6\ \mathrm{ppm}$, comprises both organic and inorganic constituents that can absorb and scatter light. Even at low concentrations, TDS has been found to significantly affect light penetration, particularly when coupled with high concentrations of chromophoric dissolved organic matter (CDOM) or fine particulates (Wibisono *et al*., 2023).

Electrical conductivity and resistivity, measured at $51.3\ \mu\mathrm{S/cm}$ and $19.3\ \mathrm{k\Omega.cm}$ respectively, reflect the electrolyte content and ion mobility within the water column. Conductivity is a measure of how many charged particles (like salts) are present in the water, which not only alter the medium’s optical density but can also serve as nucleation centers for particle aggregation which further contributes to beam attenuation (Boss *et al*., 2013).

4.3 Impact of Chemical Properties on Radiative Transfer in the Water Column

The chemical composition of the solution was determined using the Flame Spectrometer Model FP640. In aquatic systems, the concentration of dissolved nutrients significantly influences the absorption and scattering of irradiance. In this analysis, the primary constituents examined were sodium and potassium ions. Their respective concentrations were quantified by comparing the emission intensities of the samples against calibration curves constructed from standard solutions with known sodium and potassium concentrations. These calibration curves enabled accurate inference of ion concentrations within the water column, providing critical insight into the optical and chemical properties of the solution.

4.3.1 Calibration of Sodium Concentration Using Flame Emission Spectroscopy

To generate the calibration curve shown in Figure 4.2, a series of standard sodium solutions with known concentrations were analyzed using the Flame Spectrometer Model FP640. The emission intensities (W/sr) corresponding to each concentration were recorded and plotted against sodium concentration to establish a calibration reference.

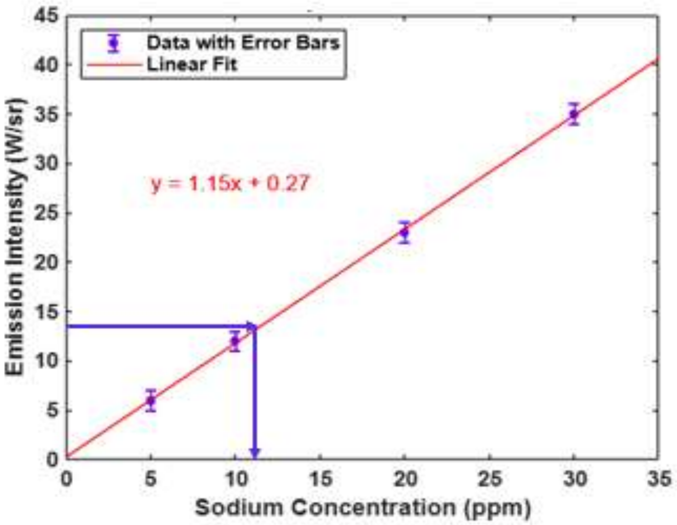

Figure 4.2: Standardized Sodium Concentration in the Water Column

A linear fit was applied to the plotted data, resulting in the equation $y = 1.15x + 0.27$, where y represents emission intensity (W/sr) and x is sodium concentration (ppm), whereby, sodium concentration was inferred to be 12 ppm, based on the calibration curve derived from standard solutions with known sodium concentrations. The fit yielded a slope of 1.15 with a standard error of 0.0152, indicating that the emission intensity increases by approximately 1.15 units per 1 ppm increase in sodium concentration. The intercept was calculated as -0.2712 and a standard error of 0.2861. An adjusted R^2 value of 0.9995 confirms an excellent correlation between concentration and intensity, validating the reliability of this method for quantifying sodium levels in aqueous samples.

4.3.2 Calibration of Potassium Concentration Using Flame Emission Spectroscopy

Quantification of potassium concentration in the sample, expressed in parts per million (ppm), was performed using flame emission spectroscopy. A series of standard solutions with known potassium concentrations were first prepared, and their corresponding emission intensities were measured using the Flame Spectrometer Model FP640. These data points were used to construct a calibration curve, which served as a reference for determining unknown concentrations as shown in Figure 4.3.

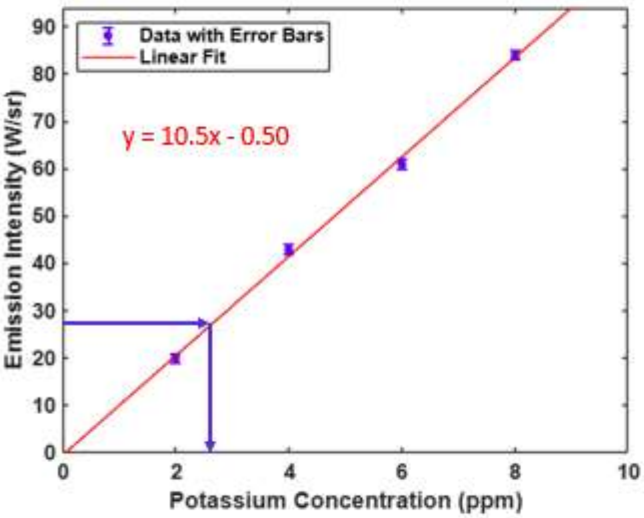

Figure 4.3: Standardized Potassium Concentration in the Water Column

A linear fit was applied to the plotted data, resulting in the equation $y = 10.5x - 0.50$, where y represents emission intensity (W/sr) and x is potassium concentration (ppm), whereby, potassium concentration was inferred to be 2.8 ppm, based on the calibration curve derived from standard solutions with known potassium concentrations. The fit yielded a slope of 10.5 with a standard error of 0.3536, indicating that the emission intensity increases by approximately 10.5 units per $1\,\text{ppm}$ increase in potassium concentration. The intercept was calculated as -0.5 and a standard error of 1.936. An adjusted R^2 value of 0.9966 confirms an excellent correlation between concentration and intensity, validating the reliability of this method for quantifying potassium levels in aqueous samples.

The observed linear relationships are highly valuable as they facilitate predictable and consistent traversal of irradiance through the medium to the target photovoltaic (PV) module. The relatively low slope values suggest a stable and predictable relationship between emission intensity of sodium and potassium concentration, which is crucial for the performance and reliability of submerged PV systems. Both physical and chemical parameters of the water column, including absorption, scattering, reflection, transmission, attenuation and fluid density, play significant roles in determining the available light intensity within the fluid column (Dera & Wozniak, 2010).

These findings are essential for understanding the optical properties of water columns and the impact of dissolved substances on light transmission. The precise measurements and strong linear correlations provide a solid foundation for predicting the behavior of submerged PV systems. The data offer critical insights into the factors affecting light attenuation in aqueous environments, which are vital for optimizing the performance of underwater solar energy systems.

4.4 Analysis of I-V Characteristics for Submerged PV Modules at Varying Depths

The I-V characteristics of the submerged photovoltaic (PV) module, measured at depths of $3, 6, 9, 12, 15$ and 18 cm, reveal critical insights into the performance of underwater solar energy systems. The data, recorded at $27.7^{\circ}\mathrm{C}$ and $12.3^{\circ}\mathrm{C}$, highlighting the impact of water depth and temperature on the electrical output of PV modules as shown in Figure 4.4. The measurements were conducted over a voltage range of approximately $10.5 - 15.0$ V, allowing for direct comparison of the electrical response under different thermal conditions.

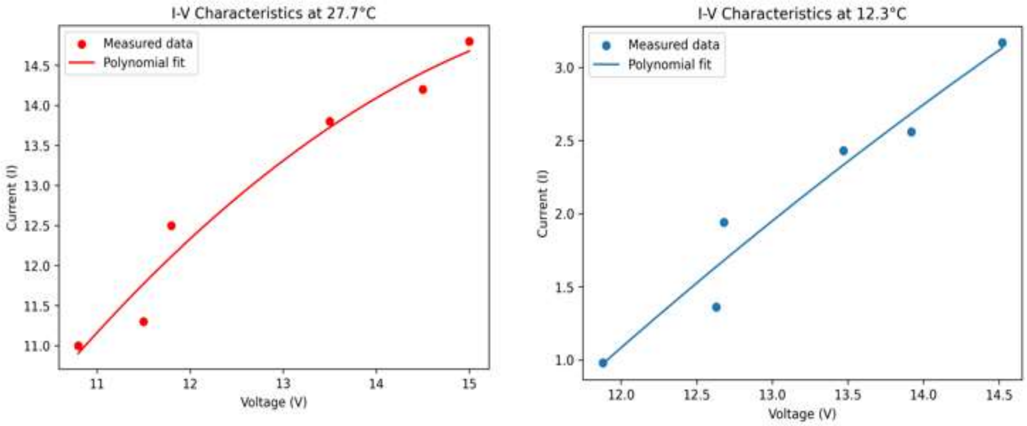

(a) (c)

Figure 4.4: The Variation in Voltage Response to Electrical Current at Two Distinct Temperatures $27.7^{o}\mathrm{C}$ and $12.3^{o}\mathrm{C}$

At an operating temperature of $27.7^{o}\mathrm{C}$, Figure 4.4 (a), the module exhibits relatively high output current, 11.0 A at 10.8 V to approximately 14.8 A at 15.0 V. The I-V relationship displays a nonlinear trend as evidenced by the curvature of the fitted polynomial. This can be attributed to internal resistive effects, junction behavior and temperature-dependent charge career dynamics, (Mulati & Timonah, 2022).

The reduced current and voltage ranges observed at $12.3^{o}\mathrm{C}$, Figure 4.4 (b), current varying from 1.0 A to 3.2 A over a comparable voltage range. The slope of the I–V curve is noticeably smaller than that observed at $27.7^{o}\mathrm{C}$, this indicates that lower temperatures exacerbate efficiency losses due to decreased charge carrier mobility and increased series resistance (Micheli *et al*., 2021). The short-circuit event observed at $12.3^{o}\mathrm{C}$ indicates that even in the absence of external load with zero terminal voltage, photogenerated charge carriers continue to contribute to current flow. This is a fundamental characteristic of PV devices, where incident irradiance generates electron–hole pairs that are driven by the internal electric field of the p–n junction, resulting in current flow independent of the external voltage under short-circuit conditions (Mulati & Timonah, 2022).

The polynomial fitting of the I-V curves underscores the complexity of PV operation underwater, where factors such as water turbidity, depth-dependent irradiance, and cooling effects play a crucial role. Previous studies have shown that water absorbs and scatters sunlight, particularly in the red and infrared spectra, reducing the effective irradiance reaching the solar cells at greater depths (Gómez-Galán *et al*., 2020). Additionally, the thermal regulation provided by water can mitigate the efficiency losses typically observed in overheated terrestrial PV systems (Siecker *et al*., 2017). However, the trade-off between cooling benefits and optical losses must be carefully balanced to optimize underwater PV performance.

These findings align with recent research on submerged silicon PV systems, which suggests that shallow deployments (≤ 10 cm) often yield the best efficiency due to sufficient light penetration while minimizing resistive losses (Rosa-Clot *et al*., 2020). Beyond this depth, the rapid decline in irradiance leads to a significant drop in power output, as confirmed by the experimental data.

4.5 Results of Power Output as a Function of the Operating Temperature with Regards to the Submersion Depth

The operating temperatures of $12.3^{\circ}\mathrm{C}$ and $27.7^{\circ}\mathrm{C}$ were achieved under controlled experimental conditions to investigate the thermal effects on submerged PV module performance. These temperatures were selected to represent a range of realistic aquatic environments, from cooler to warmer water bodies. The results demonstrate a clear inverse relationship between operating temperature and power output, consistent with the negative temperature coefficient of PV modules, as shown in Figure 4.5.

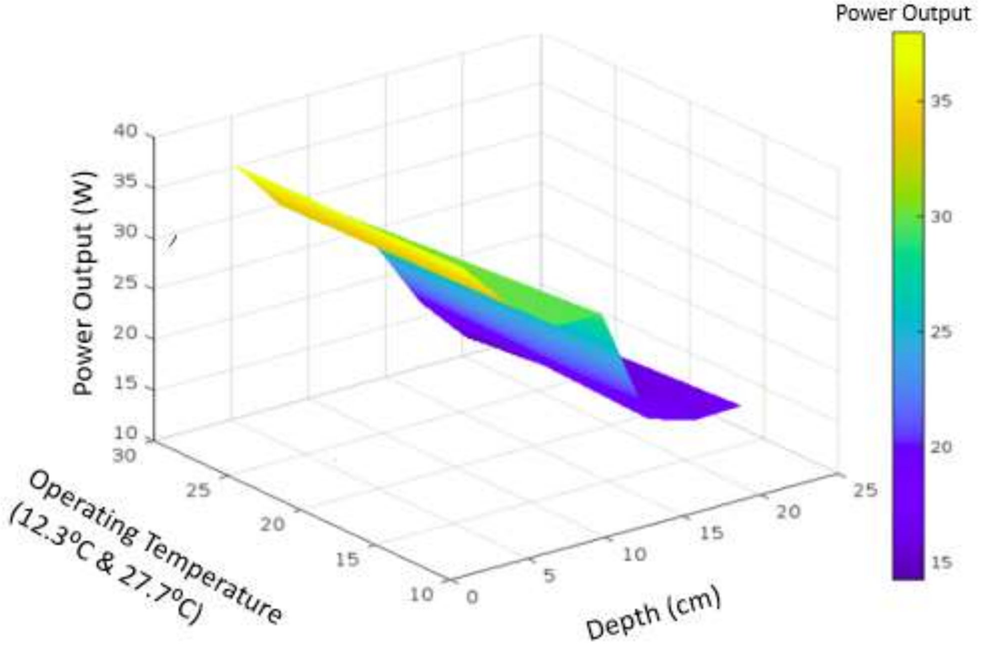

Figure 4.5: Surface Plot of Power Output as a Function of Operating Temperature and Submersion Depth

At 12.3^{o}C, the power output was consistently higher across all submersion depths, with reductions in power output becoming more pronounced as depth increased. This is attributed to the combined effects of irradiance attenuation in water and the enhanced module efficiency at lower temperatures, where reduced electron-hole recombination rates preserve open-circuit voltage (Jonasz & Fournier, 2011). This type of analysis is valuable for applications of submerged PV for autonomous systems.

Conversely, at 27.7^{o}C, the power output exhibited a steeper decline with increasing depth, indicating that higher temperatures increase the negative impact of depth on PV performance. The nonlinear interaction between temperature and depth is evident in the 3D surface plot, where the power differential between the two temperatures widens significantly at greater depths. This behavior underscores the inefficiency of heat dissipation in warmer water, which fails to adequately cool the module, leading to increased internal resistance and further power losses (Zhang *et al*., 2024; Kumar & Mishra, 2023; Bensalem *et al*., 2017; Geng *et al*., 2017).

Additionally, the warmer water does not provide sufficient cooling to mitigate the heat generated by the module. The power decline is steeper at $27.7^{\circ}\mathrm{C}$ than at $12.3^{\circ}\mathrm{C}$, indicating a more significant loss of efficiency due to higher temperatures. This behavior reflects the general observation that PV modules lose efficiency as temperatures rise beyond their optimal operating range (Berthod *et al*., 2016; Febba *et al*., 2018).

Table 4.1: The Performance of PV Module at Different Temperatures and Depth Summary

		$27.7^{o}C$			$12.3^{o}C$	
Depth	**Current (I)**	**Voltage (V)**	**Power (W)**	**Current (I)**	**Voltage (V)**	**Power (W)**
3	14.8	15.0	222.0	3.17	14.52	46.03
6	14.2	14.5	205.9	2.56	13.92	35.64
9	13.8	13.5	186.3	2.43	13.47	32.73
12	12.5	11.8	147.5	1.94	12.68	24.60
15	11.3	11.5	130.0	1.36	12.63	17.18
18	11.0	10.8	118.8	0.98	11.88	11.64

4.6 Results of Power Density as a Function of the Operating Temperature at $12.3^{\circ}\mathrm{C}$ and Submersion Depth

The irradiance attenuation profile as a function of submersion depth was analyzed under controlled water temperature conditions $(12.3^{\circ}\mathrm{C})$ to evaluate its impact on the performance of submerged photovoltaic (PV) modules. A linear regression model was applied to quantify the relationship between incident irradiance $(\mathrm{W/m^2})$ and submersion depth, as illustrated in Figure 4.6.

The first reading was carried out at, $3\ \mathrm{cm}$ depth, the measured irradiance reached a maximum value of $400\ \mathrm{W/m^2}$, consistent with the regression intercept of $409.57\ \mathrm{W/m^2}$ (y-axis at $\mathrm{d} = 3\ \mathrm{cm}$). As depth increased, a systematic reduction in irradiance was observed, declining to $360\ \mathrm{W/m^2}$ at a submersion depth of $18\ \mathrm{cm}$. The regression yielded a slope of $-2.7169\ \mathrm{W/m^2/cm}$, indicating that irradiance decreases linearly at a rate of $2.7619\ \mathrm{W/m^2}$ for every centimeter increase in depth. This attenuation is attributed to the combined effects of water absorption and scattering, which progressively diminish transmitted solar radiation as a function of depth (Berthod *et al*., 2016).

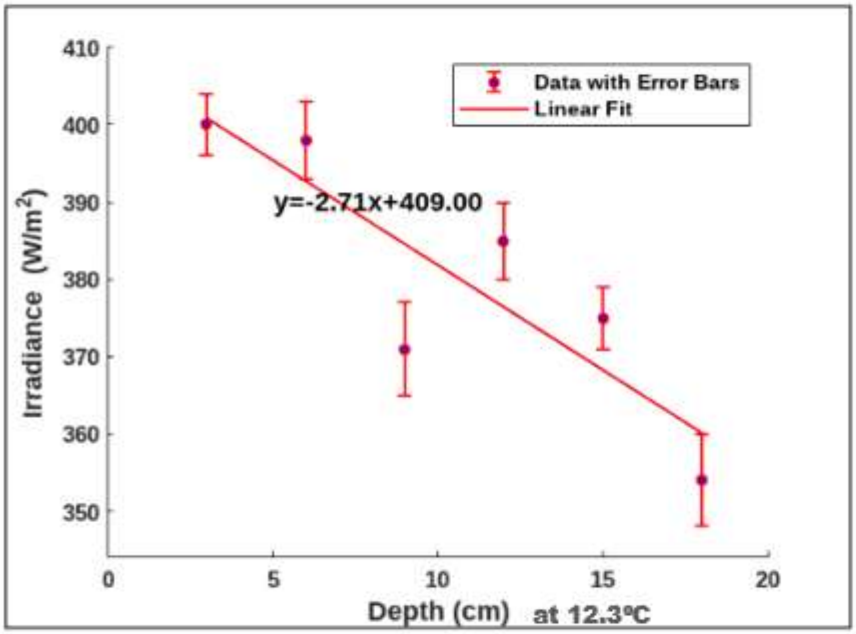

Figure 4.6: Irradiance against PV Module Depth at $12.3^{o}C$

An adjusted R-squared value of 0.80405 was extracted, indicating that 80.4% of the observed variability in irradiance can be explained by the submersion depth at $12.3^{o}\mathrm{C}$. This strong negative correlation underscores the direct influence of submersion depth on the irradiance received by the PV module (Ghimire *et al*., 2023).

To quantify the irradiance loss, the attenuation percentage was calculated using the empirical formulation expressed in equation 4.1 (Zhou *et al*., 2022):

$$\text{Percentage loss} = \left(1 - \frac{I_{(d)}}{I_o}\right)100 \quad \ldots\ldots\ldots\ldots\ldots\ldots\ldots\ldots.4.1$$

Where $\mathrm{I}_{(\mathrm{d})}$ is the final irradiance at depth $\mathrm{d} = 18$ cm, $(355\ \mathrm{W/m^2})$ and $\mathrm{I_o}$ is the initial irradiance, $\mathrm{d} = 3$ cm, $(\mathrm{I_o} = 400\ \mathrm{W/m^2})$.

For the measured depth range $(3 - 18$ cm), the irradiance loss is given by the substitution as shown:

$$\left(1 - \frac{355}{400}\right)100 = 11.25\%$$

This 11.25% reduction in irradiance over 15 cm highlights the significant role of optical attenuation in aqueous media, driven primarily by absorption and scattering mechanisms (Zhou *et al.*, 2022). The observed attenuation aligns with recent studies on submerged PV systems, where water turbidity and spectral filtering effects further modulate energy conversion efficiency (Martínez-Suárez *et al*., 2023).

The attenuation characteristics of different wavelength spectra were also examined. Longer wavelengths, which have lower energy, are absorbed more at the surface, while shorter wavelengths, with higher energy, penetrate deeper. This observation aligns with findings on nanorods as wavelength-selective absorption centers in the visible and near-infrared regions of the electromagnetic spectrum (Zhou *et al.*, 2022). For instance, exposure to 532 nm (green) light led to a temperature increase in the plasmonic nanorods sample, confirming efficient energy coupling, whereas 832 nm (NIR) light did not induce a significant temperature rise (Serna *et al*., 2023).

These findings are crucial for understanding the thermal and optical effects on submerged PV systems. The quantitative analysis of irradiance attenuation and specific wavelength absorption provides valuable insights into the performance and optimization of underwater solar energy systems.

4.7 Results of Power Density as a Function of the Operating Temperature at $\mathbf{27.7^oC}$ and Submersion Depth

Similarly, at 27.7^oC irradiance attenuation profile as a function of submersion depth was analyzed under controlled water temperature conditions to evaluate its impact on the performance of submerged PV modules. A linear regression model was applied to quantify the relationship between incident irradiance (W/m^2) and submersion depth, as illustrated in Figure 4.7, which revealed significant insights into the performance of submerged photovoltaic (PV) modules under warmer condition.

The first reading was carried out at, $3\,cm$ depth, the measured irradiance reached a maximum value of $450\,W/m^2$, consistent with the regression intercept of $449.67\,W/m^2$ (y-axis at $d = 3$ cm). As depth increased, a systematic reduction in irradiance was observed, declining to $360\,W/m^2$ at a submersion depth of $18\,cm$. The regression yielded a slope of $-6.8619\,W/m^2/cm$, indicating that irradiance decreases linearly at a rate of $6.7619\,W/m^2$ for every centimeter increase in depth. This steeper slope compared to the 12.3^oC conditions suggest a faster rate of irradiance loss with depth, highlighting that light attenuation is more pronounced at higher temperatures.

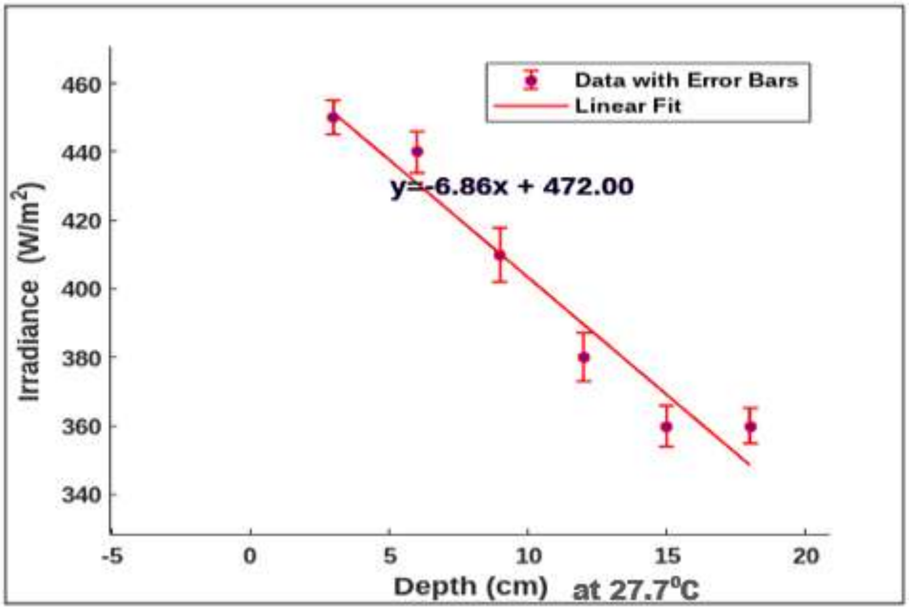

Figure 4.7: Irradiance against PV Module Depth at 27.7^{o}C

An adjusted R-squared value of 0.93206 was extracted, which demonstrates a strong correlation between depth and irradiance, 93.2% of the observed variability in irradiance being explained by depth. This strong negative correlation underscores the direct impact of submersion depth on the irradiance received by the PV module, which in turn affects the module's output.

To quantify the attenuation of irradiance in this column, the percentage loss of irradiance between 3 cm to 18 cm depth was calculated and value given by the following substitution;

$$\left(1-\frac{360}{450}\right)100=20\%$$

This indicates that 20% of the irradiance is lost over the 15 cm depth in the warmer water column. This absorption rate is 8.75% higher than that observed in the cooler water column (12.3^{o}C), demonstrating that warmer water attenuates light more significantly.

The increased attenuation in warmer water is attributed to the lower refractive index of water at higher temperatures, which causes light to bend less sharply as it passes through. This phenomenon, known as spectral attenuation, is influenced by factors such as water column purity, temperature and depth (Tan *et al.*, 2003). The selective absorption of different wavelengths of light at varying rates by the water medium plays a crucial role in this process.

These findings are essential for understanding the thermal and optical effects on submerged PV systems. The quantitative analysis of irradiance attenuation at different temperatures provides valuable insights into the performance and optimization of underwater solar energy systems.

4.8 Spectral Attenuation Characteristics and Temperature Dependence in Underwater Photovoltaic Systems

The attenuation process is further modulated by water temperature, as evidenced by experimental measurements at $12.3^{\circ}\mathrm{C}$ and $27.7^{\circ}\mathrm{C}$. From our analysis, we deduce that the irradiance within the medium is directly proportional to depth. For the water column at $27.7^{\circ}\mathrm{C}$, where 20% of the incident irradiance was lost through the column, the remaining 80% transmitted at a depth of 18 cm can be expressed as a fraction of the blue spectrum ($350 - 450$ nm), which was least attenuated. This relationship is given by the following expression:

$\mathrm{I_o} = 100\%$ of the incident irradiance,

$\mathrm{I} = 80\%\ \mathrm{I_o}$

Transmittance, $\mathrm{T} = \frac{\mathrm{I}}{\mathrm{I_o}} = 0.80$

$= [100\%\ \lambda]$

Where λ is $350 - 450$ nm.

That is for 27.7^{o}C, being that 20% of the incident irradiance was lossed through the column and the remaining 80%, transmitted at the depth, 18 cm, is expressed as a whole fraction of the blue spectrum ($350 - 450$ nm), which was least attenuated.

Similarly, for the water column at 12.3^{o}C, where 11.25% of the incident irradiance was lost, the remaining 88.75% transmitted at a depth of 18 cm is given by the expression below:

$$\mathrm{I_o} = 100\% \text{ of the incident irradiance}$$

$$\begin{aligned} &\mathrm{I} = 88.75\%\ \mathrm{I_o} \\ &\text{Transmittance, } \mathrm{T} = \frac{\mathrm{I}}{\mathrm{I_o}} = 0.8875 \\ &\quad = [100\%\ \lambda] \end{aligned}$$

Where λ is $350 - 450$ nm.

These deductions align with findings from a study on the apparent optical properties of the sea, where the measured and modeled depths of the 1% and 10% light levels were compared for different wavelengths. The model predicted higher values for the $300 - 450$ nm spectrum at the measured depth of the 10% light level compared to the 1% light level (Antoine *et al*., 2013).

4.9 Influence of Water Temperature on Irradiance Attenuation for Submerged PV Applications

The comparative analysis of irradiance propagation at two different temperatures, 12.3^{o}C and 27.7^{o}C, provides valuable insights into the influence of temperature on the performance of submerged photovoltaic (PV) modules. Figure 4.8 illustrates the variation in irradiance with depth at two different water temperatures, 12.3^{o}C and 27.7^{o}C, providing critical insights into how temperature influences irradiance propagation in submerged environments. At $12.3^{\mathrm{o}}\mathrm{C}$, the irradiance decreases gradually and exhibits a near-linear trend, suggesting relatively stable attenuation across the water column. In contrast, the $27.7^{\mathrm{o}}\mathrm{C}$ curve reveals a steeper, nonlinear decline that follows a second-order polynomial pattern. This indicates a more rapid reduction in irradiance with increasing depth, reflecting heightened scattering and absorption of light energy at elevated temperatures.

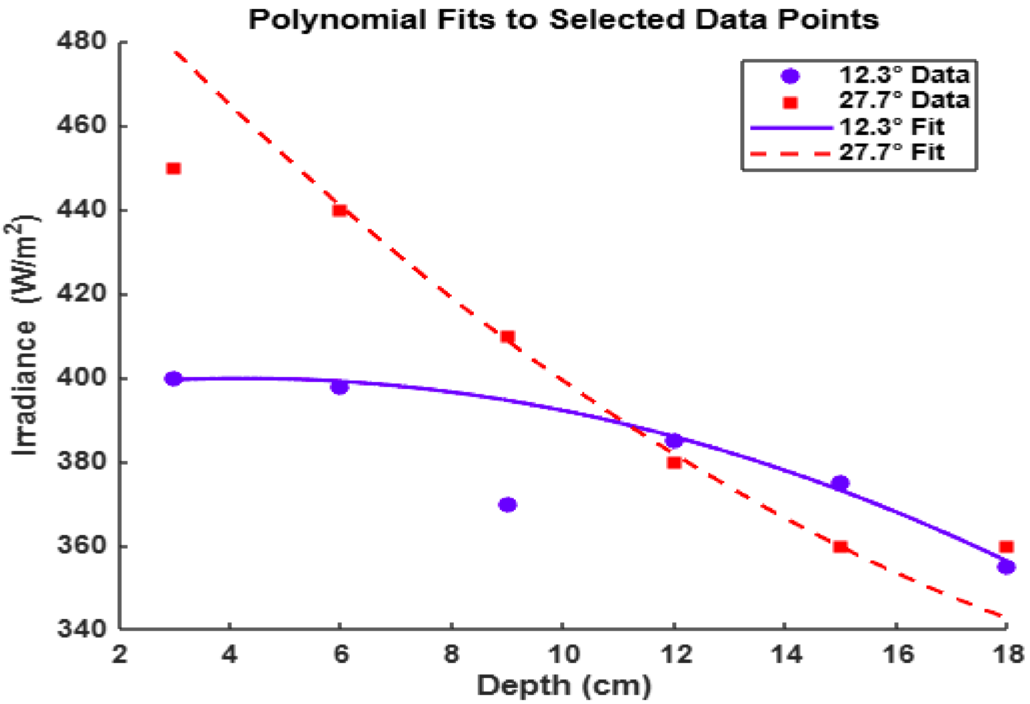

Figure 4.8: Comparison of Irradiance against Depth at $12.3^{\mathrm{o}}\mathrm{C}$ and $27.7^{\mathrm{o}}\mathrm{C}$

A comparative analysis of the fitted polynomial models highlights these differences quantitatively. At $27.7^{\mathrm{o}}\mathrm{C}$, the irradiance begins at a higher intercept value of $450\ \mathrm{W/m^2}$, compared to $400\ \mathrm{W/m^2}$ at $12.3^{\mathrm{o}}\mathrm{C}$, a difference of approximately 12.5%. This elevated initial irradiance at the higher temperature may be attributed to increased molecular kinetic activity, allowing for greater initial absorption of radiant energy. The attenuation rate is further distinguished by the model coefficients: for $27.7^{\mathrm{o}}\mathrm{C}$, the first-order and second-order coefficients are -10.2074 and 0.7857, respectively, indicating a sharp and accelerated decrease in irradiance with depth. Conversely, the coefficients at $12.3^{\mathrm{o}}\mathrm{C}$ are -5.2841 and 0.1388, signifying a more gradual decay.

The adjusted R-squared values underscore the consistency of these trends, with the model for $27.7^{\mathrm{o}}\mathrm{C}$ achieving a strong fit ($\mathrm{R}^2 = 0.9836$), whereas the $12.3^{\mathrm{o}}\mathrm{C}$ model demonstrates greater variability in the data ($\mathrm{R}^2 = 0.6148$). These results suggest that higher temperatures induce greater fluctuations in irradiance attenuation, likely due to thermally driven changes in the intermolecular structure of water. Increased molecular motion at $27.7^{\mathrm{o}}\mathrm{C}$ enhances the scattering and absorption of light, while at $12.3^{\mathrm{o}}\mathrm{C}$, reduced thermal activity and tighter molecular packing allow irradiance to penetrate deeper with less dispersion.

These temperature-dependent optical behaviors are consistent with prior findings, which link increased temperature to intensified molecular vibration and light scattering in aquatic environments (Katsukura *et al*., 2017). The findings highlight the importance of considering temperature effects when designing and optimizing submerged PV systems. The detailed analysis of irradiance attenuation at different temperatures provides critical insights for improving the efficiency and reliability of underwater solar energy systems, making this discussion highly relevant for scientific research and practical applications in renewable energy technologies.

4.10 Effects of Temperature on Intermolecular Vibrational and Rotational Transitions and their Impacts on Irradiance Transmission

Results have shown that the cooler water column at $12.3^{\mathrm{o}}\mathrm{C}$ transmitted 88.75% of incident irradiance at 18 cm, while the water column at $27.7^{\mathrm{o}}\mathrm{C}$ transmitted only 80%. This difference highlights the impact of temperature on light attenuation due to variations in absorption and scattering dynamics. In an underwater environment, light attenuation is largely affected by absorption and scattering mechanisms. Absorption converts light energy into heat, primarily through vibrational and rotational transitions of water molecules, while scattering deflects light in multiple directions due to particle interactions and molecular structure. Temperature plays a critical role in these processes as it influences molecular dynamics and consequently the balance between absorption and scattering (Röttgers *et al*., 2014).

The cooler water column, $12.3^{\circ}\mathrm{C}$, demonstrated higher irradiance transmittance at depth of 18 cm as compared to the water column at $27.7^{\circ}\mathrm{C}$, which recorded 80%. This aligns with findings by (Röttgers *et al*., 2014; Lee *et al*., 2014), who noted that cooler water exhibits lower absorption rates across certain wavelengths, particularly in the visible spectrum and near-infrared wavelengths. This implies that incident irradiance can travel further before being absorbed. At lower temperature, reduced molecular vibrations implies that light absorption processes are less active, allowing a greater percentage of irradiance to propagate through water (Röttgers *et al*., 2014).

Conversely, in the cooler water column at $12.3^{\circ}\mathrm{C}$, the molecular structure remains more stable compared to the warmer water column, resulting in lower absorption rates, thus higher irradiance values at greater depths. As temperature increases, molecular vibration becomes more pronounced, leading to higher absorption coefficients. As a result, cooler water columns allow more light to penetrate before being absorbed. Additionally, the cooler column has a higher refractive index than the warmer column, this phenomenon reduces the angle of refraction and critical angle in the cooler column, thus, allowing for light to penetrate deeper into the cooler column rather than spreading out. For instance, it was demonstrated that as temperature rises, the absorption rate significantly increases, which results in reduced irradiance penetration in warmer water columns (Röttgers *et al*., 2014). This aligns with our findings that the cooler water, $12.3^{\circ}\mathrm{C}$, has higher percentage, 88.75%, of irradiance at greater depths, 18 cm, compared to the warmer column, $27.7^{\circ}\mathrm{C}$, which registered a lower percentage, 80%, at the same depth. This is due to pronounced absorption at higher temperature.

Absorption increases with temperature due to enhanced molecular rotational and vibrational energy states in water molecules. At $27.7^{\circ}\mathrm{C}$, water molecules have increased kinetic energy, leading to its higher capacity to absorb infrared spectrum, the longer wavelength, due to alterations in molecular structure and dynamics. This is particularly evident in the absorption spectra of water, where certain wavelengths become more effectively absorbed at higher temperatures. For instance, the absorption of thermal energy is influenced by the vibrational modes of water molecules which becomes more active as the temperature rises, leading to enhanced absorption of the infrared radiation (Amber *et al*., 2018).

Additionally, higher temperatures, $27.7^{\mathrm{o}}\mathrm{C}$, results in increased molecular motion within the water column. This heightened activity can facilitate effective interactions between incident irradiance and water molecules, thereby increasing overall absorption efficiency. The kinetic energy of the molecules at elevated temperatures allows for more frequent collisions and interactions with photons, which enhances the likelihood of energy transfer from the radiation to the water (Ishizaki *et al*., 2010; Amber *et al*., 2018).

Based on the observed results, we can draw an analogy regarding the potential application of submerged PV modules in amphibious drones. The findings suggest that this experimental setup may be more suitable for deployment in dam environments rather than oceanic settings. This inference is based on several key factors: Dam waters exhibit lower average temperatures than the oceanic medium, this is due to the vast surface area of the oceans that allows them to absorb and retain more heat energy, and from our results we have observed that at cooler temperature, the shorter wavelength spectrum penetrates more effectively than in warmer medium. This is also shown by the difference in the value of irradiance at $18\ \mathrm{cm}$ depth, at $12.3^{\mathrm{o}}\mathrm{C}$ a value of $355\ \mathrm{W/m^2}$ was recorded while at $27.7^{\mathrm{o}}\mathrm{C}$ it was $360\ \mathrm{W/m^2}$. Additionally, dam water temperatures are generally more stable and predictable than ocean temperatures, scientifically, more consistent temperatures allow for better calibration of sensors and more reliable data collection.

Consequently, dams often have more controlled and consistent depths compared to the highly variable depths of oceans. This could allow for more predictable and optimized positioning of submerged amphibious drones incorporated with the PV modules.

CHAPTER FIVE

CONCLUSION AND RECOMMENDATIONS

5.1 Conclusion

This study investigated the influence of temperature on irradiance attenuation and energy capture in a submerged water column, with specific focus on the performance of submerged photovoltaic (PV) systems under varying thermal conditions. By examining irradiance decay profiles at $12.3^{o}\mathrm{C}$ and $27.7^{o}\mathrm{C}$, analyzing attenuation coefficients and quantifying power output at different depths, the research aimed to assess the feasibility of harnessing solar energy for powering aquatic technologies, such as amphibious drones. The outcomes provide valuable insights into the interaction between thermal properties of water and light propagation, crucial for optimizing submerged solar energy systems.

The decay of irradiance within the water column was found to follow an exponential relationship with the attenuation coefficient. This confirms that light intensity decreases non-linearly with depth, which has important implications for designing and deploying PV systems underwater. Understanding this exponential decay is critical for predicting energy availability at various depths.

Sample A, with an attenuation coefficient of $\mathrm{k} = 0.2\ \mathrm{m}^{-1}$ exhibited a notably rapid decay in irradiance, attributed to the higher concentration of dissolved substances. These substances enhance light absorption and scattering, thereby reducing the amount of irradiance reaching deeper layers. This demonstrates that water composition significantly impacts light transmission and, consequently, the performance of submerged energy systems.

It was also observed that the power harnessed from within the water column is directly proportional to depth. At $12.3^{o}\mathrm{C}$, the power output was $46.03\ \mathrm{W}$ at the surface and reduced to $11.64\ \mathrm{W}$ at a depth of $18\ \mathrm{cm}$, while at $27.7^{o}\mathrm{C}$, the power output recorded at the surface was $222.0\ \mathrm{W}$ and decreased to $118.8\ \mathrm{W}$ at $18\ \mathrm{cm}$ depth. This gradient illustrates the diminishing energy potential with increasing depth and underscores the importance of optimizing the placement of PV modules within the water column for maximum efficiency.

Temperature was shown to affect irradiance transmission significantly. At $27.7^{\circ}\mathrm{C}$, the irradiance transmitted through the column was 80%, while at $12.3^{\circ}\mathrm{C}$, the value transmitted was 88.75%. This trend suggests that cooler water, due to reduced intermolecular activity and scattering, permits deeper light penetration, which can enhance the performance of submerged PV systems under lower thermal conditions.

Based on these findings, it is concluded that sufficient irradiance and energy can be harnessed within a water column to power practical aquatic applications. The energy levels observed are adequate to support operations of small-scale technologies, such as amphibious drones, confirming the viability of underwater solar harvesting systems in renewable energy deployment.

5.2 Recommendations

The study findings are significant for stakeholders in marine research, surface ocean exploration, remote sensing, water quality monitoring, ocean surface surveillance and oceanography. The findings are particularly relevant for designing amphibious drones that are powered by photovoltaic systems. Drawing from these finds, the researcher recommends that;

1. Research could also delve into how different types of suspended matter particles; organic against inorganic, affect light attenuation.
2. Changes in temperature and salinity also affect water density and its ability to scatter or absorb light. Extended research could model how temperature gradients and salinity variations affect irradiance profile across different depths.

REFERENCES

ACS Applied Materials & Interfaces. (2023). Biofouling-resistant coatings for underwater photovoltaics. *ACS Applied Materials & Interfaces,* ***15***(12), 15678–15691.

Advanced Energy Materials. (2023). Perovskite solar cells for underwater applications. *Advanced Energy Materials,* ***13***(15), 2203456.

Akyildiz, I. F., Pompili, D., & Melodia, T. (2021). Underwater acoustic sensor networks: Research challenges. *IEEE Communications Surveys & Tutorials,* ***23***(2), 1370–1387.

Al-Ashouri, A., Köhnen, E., Li, Z., Magomedov, A., Hempel, H., Caprioglio, P., … Leo, K. (2023). Monolithic perovskite/silicon tandem solar cells with >33% efficiency. *Nature Energy*, ***8***(3), 123–134..

Amber, K., Mahmoud, M. S., & Khalil, E. E. (2018). Effect of temperature on the absorption characteristics of water for solar energy applications. Solar Energy, 162, 45–52.

Antoine, D., Hooker, S. B., Bélanger, S., Matsuoka, A., & Babin, M. (2013). Apparent optical properties of the Canadian Beaufort Sea–Part 1: Observational overview and water column relationships. *Biogeosciences,* ***10***(7), 4493-4509.

Bensalem, S., Chegaar, M., & Herguth, A. (2017). Band gap dependence with temperature of semiconductors from solar cells electrical parameters. *Current Applied Physics*, ***17***(1), 55-59.

Benway, H. M., Lorenzoni, L., White, A. E., Fiedler, B., Levine, N. M., Nicholson, D. P., ... & Letelier, R. M. (2019). Ocean time series observations of changing marine ecosystems: an era of integration, synthesis, and societal applications. *Frontiers in Marine Science*, ***6***, 393.

Berthod, C., Strandberg, R., Yordanov, G.H., Beyer, H.G., Odden, J.O., 2016. On the variability of the temperature coefficients of mc-si solar cells with irradiance. Energy Procedia, 92, 2–9.

Boss, E., Slade, W. H., & Hill, P. S. (2013). Effect of particulate aggregation in aquatic environments on light scattering and beam attenuation. *Applied Optics*, ***52***(12), 2786–2796.

Cazzaniga, R., Cicu, M., Rosa-Clot, M., Rosa-Clot, P., Tina, G. M., & Ventura, C. (2018). Floating photovoltaic plants: Performance analysis and design solutions. *Renewable and Sustainable Energy Reviews* ***81***, 1730-1741.

Charette, M. A., & Smith, W. H. (2010). The volume of Earth's ocean. *Oceanography*, ***23***(2), 112-114.

Chen, X., & Lee, H. (2023). "Impedance matching in underwater acoustic energy transfer". *IEEE Transactions on Ultrasonics, Ferroelectrics, and Frequency Control*, ***70***(2), 145-152.

Chen, X., Huang, Y., Lin, D., & Zhao, F. (2023). Advanced battery technologies for autonomous underwater vehicles. *Journal of Power Sources* ***555***, 232397.

Chen, X., Wang, Z. L., & Liu, G. (2022). Hybridized nanogenerator networks for blue energy harvesting. *Nano Energy* ***100***, 107498.

Dalin, P., Svensson, G., Liu, Y., & Kim, H. (2024). Thermo-optic effects in aquatic photonics. *Nature Water,* ***2***(1), 45–53.

Dehwah, A. H., Wicaksono, A., & Al-Ghamdi, S. G. (2022). Investigating floating solar PV systems: A review of status, barriers, and future prospects. *Renewable and Sustainable Energy Reviews* ***160***, 112279.

Dehwah, A. H., Zhao, F., & Wang, H. (2023). Performance of organic solar cells under simulated underwater light conditions. *Applied Energy* ***332***, 120543.

Dera, J., & Wozniak, B. (2010). Solar radiation in the Baltic Sea. *Oceanologia*, ***52***(4).

Dierssen, H. M., Chlus, A., & Russell, B. (2020). Underwater light field patterns and implications for image-based remote sensing. *Optics Express,* ***28***(5), 6787–6804.

Dierssen, H., Zimmerman, R. C., Leathers, R. A., & Davis, C. O. (2021). Optical properties of coastal and ocean waters. *Limnology and Oceanography,* ***66***(3), 987–1004.

Duncan, E., Jamieson, A. J., Stevenson, P., & McKinnon, A. D. (2021). High-resolution seabed mapping in deep-water search operations. *Marine Technology Journal,* ***55***(3), 45–60.

Embury, O., Merchant, C. J., Good, S. A., Rayner, N. A., Høyer, J. L., Atkinson, C., ... & Donlon, C. (2024). Satellite-based time-series of sea-surface temperature since 1980 for climate applications. *Scientific Data*, ***11***(1), 326.

Enangati, N. K., Nallapaneni, L. A., Kolli, K. S., & Banerjee, R. (2022). A review on renewable energy harvesting from marine environment using advanced materials and system integration strategies. *Renewable and Sustainable Energy Reviews,* ***156***, 111992.

Fébba, D. M., Rubinger, R. M., Oliveira, A. F., & Bortoni, E. C. (2018). Impacts of temperature and irradiance on polycrystalline silicon solar cells parameters. *Solar Energy* ***174***, 628-639.

Fischer, A. C., Rinderknecht, S., & Wagner, S. (2021). Spectral matching of photovoltaic materials for underwater energy harvesting. *Journal of Photonics for Energy,* ***11***(2), 022003.

Geng, P., Li, W., Zhang, X., Zhang, X., Deng, Y., & Kou, H. (2017). A novel theoretical model for the temperature dependence of band gap energy in semiconductors. *Journal of Physics D: Applied Physics*, ***50***(40),

Ghimire, S., Raval, S., Maharjan, S., & Muthu Mariappan, C. (2023). Depth-dependent PV performance in aquatic environments. *Renewable Energy Reviews*, ***54***(17), 5392–5401.

Gómez-Galán, J. A., Sánchez-Pérez, M., & García-Sánchez, F. J. (2020). Performance assessment of underwater photovoltaic modules under realistic operating conditions. *Renewable Energy*, 162, 1893-1902.

Guan, S., Qu, F., & Qiao, F. (2023). United Nations Decade of Ocean Science for Sustainable Development (2021-2030): From innovation of ocean science to science-based ocean governance. *Frontiers in Marine Science*, *9*, 1091598.

Ishizaki, T., Yasui, T., & Arakawa, M. (2010). Temperature-dependent optical absorption and scattering properties of water for near-infrared laser applications. *Applied Optics*, ***49***(3), 641–646.

Jäger, K., Paetzold, U. W., & Rau, U. (2021). Perovskite and organic solar cells: A comparative review. *Advanced Energy Materials*, ***11***(15), 2002771.

Janek, J., & Zeier, W. G. (2023). "A solid future for battery development". *Nature Energy*, ***8***(3), 230-240.

Jansen, M., Thompson, D., Roberts, G., & Liu, Y. (2020). Autonomous underwater vehicles in deep-sea search operations. *IEEE Journal of Oceanic Engineering,* ***45***(2), 210–225.

Jiang, T., He, Y., & Li, Y. (2022). Radiative transfer modeling of solar irradiance in turbid water for aquatic PV applications. *Solar Energy*, 243, 123–135.

Johnson, M., & Patel, R. (2022). Hydrodynamics of underwater cables. *Ocean Engineering*, 245, 110402.

Johnson, M., Wang, T., El-Sayed, A., & Rivera, L. (2023). Adaptive optics for underwater laser power transmission. *Optics Express*, ***31***(4), 6782–6795.

Jonasz, M., & Fournier, G. (2011). Light scattering by particles in water: theoretical and experimental foundations. Elsevier.

Katsukura, H., Miyata, T., Shirai, M., Matsumoto, H., & Mizoguchi, T. (2017). Estimation of the molecular vibration of gasses using electron microscopy. *Scientific Reports*, ***7***(1), 16434.

Katzschmann, R. K., DelPreto, J., MacCurdy, R., & Rus, D. (2018). Exploration of underwater life with an acoustically controlled soft robotic fish. *Science Robotics*, ***3***(16).

Kavanaugh, M. T., Bell, T., Catlett, D., Cimino, M. A., Doney, S. C., Klajbor, W., ... & Siegel, D. A. (2021). Satellite remote sensing and the marine biodiversity observation network. *Oceanography*, ***34***(2), 62-79.

Keow, A. L. J., Zuo, W., Ghorbel, F., & Chen, Z. (2022). Reversible fuel cell enabled underwater buoyancy control. *Mechatronics* ***86***, 102865.

Kinsey, J. C., Yoerger, D. R., & Jakuba, M. V. (2016). Autonomous underwater vehicle operations in the deep ocean. *Annual Review of Marine Science* ***8***, 175–198.

Kirk, J. T. O. (2011). Light and Photosynthesis in Aquatic Ecosystems (3rd ed.). *Cambridge University Press*.

Kumar, A., & Mishra, S. (2023). "Temperature-dependent performance degradation in underwater solar cells." *Solar Energy Materials and Solar Cells*, 252, 112198.

Kumar, M., Patel, S., & Sharma, R. (2023). Design and optimization of hybrid renewable energy systems for ocean monitoring platforms. *Applied Energy*, ***331***, 120387.

Kumar, N.M. & Rosen, M.A. (2018). Performance Assessment of Solar PV Modules Under Static and Dynamic Conditions. *Energy Reports,* 4, 364–370.

Kumar, R., & Rosen, M. A. (2023). "Advances in PV system design and optimization." *Renewable and Sustainable Energy Reviews*, 172, 113045.

Lee, S., & Park, J. (2023). "Underwater optical power beaming: Challenges and solutions". *Applied Optics,* ***62***(10).

Lee, Z., Du, K., Arnone, R., Liew, M., & Ma, R. (2015). Penetration of solar radiation in the upper ocean: A numerical model for oceanic and coastal waters. *Journal of Geophysical Research: Oceans,* ***120***(7), 4799–4814.

Lee, Z., Casey, B., Arnone, R., Weidemann, A., & Davis, C. (2022). Remote sensing of aquatic light fields. *Journal of Geophysical Research: Oceans,* ***127***(4).

Levin, L. A., & Le Bris, N. (2015). The deep ocean under climate change. *Science,* ***350***(6262), 766-768.

Li, C., Wang, J., Liu, F., & Zhang, Z. (2023). Flexible and semitransparent organic photovoltaics for marine applications. *Advanced Energy Materials,* ***13***(15), 2203456.

Li, X., Zhang, Y., Chen, W., & Liu, J. (2019). Fill factor losses in silicon photovoltaics: A comparative analysis. *Solar Energy Materials and Solar Cells* ***191***, 1–9

Lingam, M., & Loeb, A. (2020). Constraints on Aquatic Photosynthesis for Terrestrial Planets around Other Stars. *The Astrophysical Journal Letters,* ***889***(1), 15.

Liu, Y., Wang, Q., & Gao, F. (2020). Environmental effects on FPV performance: Optical and thermal perspectives. *Energy Conversion and Management*, 225, 113403.

Luque, A., & Hegedus, S. (Eds.). (2011). *Handbook of photovoltaic science and engineering*. John Wiley & Sons.

Manthiram, A. (2020). "Lithium-sulfur batteries". *Nature Reviews Materials*, ***5***(3), 186-202.

Marine Nuclear Technology. (2023). "Compact reactor designs for AUV applications". ***45***(2), 112-125

Martínez-Suárez, A., Delgado-Torres, A. M., Pérez-García, M., & Ríos-Moreno, G. J. (2023). Turbidity effects on the performance of submerged photovoltaic systems. *Solar Energy Materials and Solar Cells* ***251***, 112065

Marzouk, O. A. (2025). Summary of the 2023 Report of TCEP (Tracking Clean Energy Progress) by the International Energy Agency (IEA), and Proposed Process for Computing a Single Aggregate Rating. In *E3S Web of Conferences* ***601***, 00048).

Masuko, K., et al. (2023). "High-efficiency silicon heterojunction solar cells: Recent progress and future prospects." *Advanced Energy Materials*, ***13***(4), 2203456.

Mayer, L., Jakobsson, M., Allen, G., Dorschel, B., Falconer, R., Ferrini, V., ... & Weatherall, P. (2018). Advances in seafloor mapping. *Oceanography*, ***31***(1), 32–45.

Mellit, A., Kalogirou, S. A., Massi Pavan, A., & Benghanem, M. (2023). Artificial intelligence for photovoltaic systems: A comprehensive review. *Applied Energy*, ***331***, 120356.

Micheli, L., Fernández, E. F., & Almonacid, F. (2021). Temperature coefficients of perovskite solar cells under real-world conditions. *Solar Energy Materials and Solar Cells*, 230, 111265.

Moradi, M., Arabi, B., Hommersom, A., van der Molen, J., & Samimi, C. (2023). Radiative transfer model for quality control of above-water hyperspectral downwelling irradiance measurements. *Remote Sensing of the Ocean, Sea Ice, Coastal Waters, and Large Water Regions **12728***, 109-126.

Mulati, D. M., & Soita, T. (2022). Solar Solutions for the Future. In *Recent Advances in Multifunctional Perovskite Materials*.

Nivedhitha, D., Karthik, D., & Sakthivel Murugan, S. (2022). Localization systems for autonomous operation of underwater robotic vehicles: A survey. In *OCEANS 2022-Chennai*, 1-8.

Paull, C. K., Ussler, W., Lundsten, E., Anderson, K., Gwiazda, R., & Ruppel, C. (2018). Deepwater AUV navigation challenges. *Marine Geophysical Research*, ***39***(1–2), 85–102.

Radiation Protection Dosimetry. (2023). "Radiation safety in underwater nuclear systems". ***199***(3), 234-245.

Ramirez-Llodra, E., Brandt, A., Danovaro, R., De Mol, B., Escobar, E., German, C. R., ... & Vecchione, M. (2010). Deep, diverse and definitely different: unique attributes of the world's largest ecosystem. *Biogeosciences*, ***7***(9), 2851-2899.

Reul, N., Fournier, S., Boutin, J., Hernandez, O., Maes, C., Chapron, B., ... & Delwart, S. (2014). Sea surface salinity observations from space with the SMOS satellite: A new means to monitor the marine branch of the water cycle. *Surveys in Geophysics **35***, 681-722.

Röhr, J. A., Lipton, J., Kong, J., Maclean, S. A., & Taylor, A. D. (2020). Efficiency limits of underwater solar cells. *Joule*, ***4***(4), 840–849.

Röhr, J. A., Sartor, B. E., Duenow, J. N., Qin, Z., Meng, J., Lipton, J., ... & Taylor, A. D. (2022). Identifying optimal photovoltaic technologies for underwater applications. *Iscience*, ***25***(7).

Rosa-Clot, M., Rosa-Clot, P., Tina, G. Á., & Scandura, P. F. (2010). Submerged photovoltaic solar panel: SP2. *Renewable Energy*, ***35***(8), 1862-1865.

Rosa-Clot, M., Tina, G. M., & Nizetic, S. (2020). *Submerged photovoltaic systems: A review of challenges, solutions, and prospects*. Applied Energy, 278, 115648.

Röttgers, R., McKee, D., & Utschig, C. (2014). Temperature and salinity correction coefficients for light absorption by water in the visible to infrared spectral region. *Optics Express*, ***22***(21), 25093–25108.

Rudnick, D. L. (2016). Ocean research enabled by underwater gliders. *Annual review of marine science*, ***8***(1), 519-541.

Ryabinin, V., Barbière, J., Haugan, P., Kullenberg, G., Smith, N., McLean, C., ... & Rigaud, J. (2019). The UN decade of ocean science for sustainable development. *Frontiers in Marine Science*, ***6***, 470.

Serna-Gallén, P., Beltrán-Mir, H., & Cordoncillo, E. (2023). Practical guidance for easily interpreting the emission and physicochemical parameters of Eu3+ in solid-state hosts. *Ceramics International*, ***49***(24), 41078-41089.

Shang, Y., Jacinthe, P. A., Li, L., Wen, Z., Liu, G., Lyu, L., ... & Song, K. (2021). Variations in the light absorption coefficients of phytoplankton, non-algal particles and dissolved organic matter in reservoirs across China. *Environmental Research* ***201***, 111579.

Shao, J., Jiang, T., & Wang, Z. (2020). Theoretical foundations of triboelectric nanogenerators (TENGs). *Science China Technological Sciences*, ***63***(7), 1087-1109.

Shirvan, K., et al. (2021). "Underwater SMRs for autonomous vehicle propulsion". *Nuclear Engineering and Design,* 380, 111234.

Siecker, J., Kusakana, K., & Numbi, B. P. (2017). *A review of solar photovoltaic systems cooling technologies*. Renewable and Sustainable Energy Reviews, 79, 192-203.

Singh, P., Kumar, A., Sharma, R., & Lee, C. (2020). Efficiency metrics for submerged photovoltaic modules. *IEEE Journal of Photovoltaics,* ***10***(2), 502–510.

Skoplaki, E. & Palyvos, J.A. (2019). On the Temperature Dependence of Photovoltaic Module Electrical Performance. Solar Energy, 183, 211-217.

Smith, T., & Johnson, R. (2022). "High-efficiency inductive power transfer for underwater applications". *IEEE Journal of Oceanic Engineering,* ***47***(1), 234-245.

Smith, T., Johnson, R., Chen, L., & Patel, S. (2021). High-efficiency underwater power transmission. *IEEE Transactions on Power Delivery,* ***36***(2), 987–995.

Solonenko, M. G., & Mobley, C. D. (2015). Inherent optical properties of Jerlov water types. *Applied optics*, ***54***(17), 5392-5401.

Stone, W., Fletcher, R., McLeod, R., & Chen, Y. (2021). Probability of detection models for deep-ocean searches. *Journal of Underwater Acoustics,* ***71***(4), 512–530.

Tan, M., Poon, W., & Zhang, R. (2023). Thermo-optic effects in water for photonic energy conversion. Optics Express, ***31***(4), 6789-6805.

Tarascon, J. M., & Armand, M. (2022). "Issues and challenges facing rechargeable lithium batteries". *Materials Today,* 44, 28-43.

Trowbridge, J., Weller, R., Kelley, D., Dever, E., Plueddemann, A., Barth, J. A., & Kawka, O. (2019). The ocean observatories initiative. *Frontiers in Marine Science, 6*, 74.

Ventura, D., Bonifazi, A., Gravina, M. F., Belluscio, A., & Ardizzone, G. (2018). Mapping and classification of ecologically sensitive marine habitats using unmanned aerial vehicle (UAV) imagery and object-based image analysis (OBIA). *Remote Sensing*, ***10****(*9), 1331.

Wang, H., Liu, J., Chen, D., & Zhang, Y. (2022). Acoustic impedance matching in marine energy transfer. *Journal of the Acoustical Society of America*, ***151***(3), 1892–1901.

Wang, H., Lin, Z., & Xu, S. (2023). Sustainable energy harvesting for ocean monitoring using pressure-tolerant photovoltaic systems. *Nature Sustainability*, ***6***(4), 456–468.

Weaver, A., Johnson, M., Patel, R., & Singh, N. (2023). Radioisotope power systems for deep-sea exploration. *IEEE Aerospace Conference Proceedings*, 1–9.

Wibisono, A. D., Hardi, S. M., & Sari, N. P. (2023). Characterization of Optical Properties in Coastal Waters Based on In Situ Measurements and Remote Sensing Techniques. *Journal of Marine Science and Engineering*, ***11***(2), 212.

Wölfl, A. C., Snaith, H., Amirebrahimi, S., Devey, C. W., Dorschel, B., Ferrini, V., ... & Wigley, R. (2019). Seafloor mapping–the challenge of a truly global ocean bathymetry. *Frontiers in Marine Science*, *6*, 283.

Wynn, R. B., Huvenne, V. A. I., Le Bas, T. P., Murton, B. J., Connelly, D. P., Bett, B. J., ... & Bull, J. M. (2014). Challenges in deep-ocean search operations. *Deep-Sea Research Part II: Topical Studies in Oceanography* ***104***, 4–17.

Yang, S., Liu, P., & Lim, T. H. (2023). IoT-based underwater robotics for water quality monitoring in aquaculture: A survey. In H. Kim et al. (Eds.), *Proceedings of the International Conference on Robot Intelligence Technology and Applications*, 32–42.

Yi, J., Zhang, G., Yu, H., & Yan, H. (2024). Advantages, challenges and molecular design of different material types used in organic solar cells. *Nature Reviews Materials*, ***9***(1), 46-62.

Yuan, J., Zhang, Y., & Zou, Y. (2022). Molecular engineering for high-efficiency organic solar cells. *Science, **376***(6596), 1131–1135.

Yuh, J., Marani, G., & Blidberg, D. R. (2011). Applications of marine robotic vehicles. *Intelligent service robotics **4***, 221-231.

Zang, H., Liu, X., & Mobley, C. D. (2022). Underwater light propagation and spectral optimization for marine photovoltaics. *Optics Express, **30***(5), 6522–6534.

Zereik, E., Bibuli, M., Mišković, N., Ridao, P., & Pascoal, A. (2018). Challenges and future trends in marine robotics. *Annual Reviews in Control **46***, 350-368.

Zhang, G., Liu, Y., Chen, H., Wang, X., & Li, J. (2023). Graphene-encapsulated sulfur cathodes for marine batteries. *ACS Nano, **17***(4), 3456–3468.

Zhang, G., Li, J., Liu, F., Wang, J., & Chen, Y. (2023). High-efficiency underwater organic photovoltaics for self-powered marine sensors. *Nature Energy, **8***(4), 312–325.

Zhang, G., Li, M., & Zhu, H. (2022). Light harvesting and weak-light performance in organic photovoltaics. *Advanced Materials, **34***(22), 2108345.

Zhang, H. L., Van Gerven, T., Baeyens, J., & Degrève, J. (2014). Photovoltaics: Reviewing the European feed-in tariffs and changing PV efficiencies and costs. *The Scientific World Journal*, ***2014***(1), 404913.

Zhang, X., Wu, L., Chen, Y., & Zhao, Q. (2020). Temperature-dependent light scattering in aqueous media. *Journal of Physical Chemistry B*, ***124***(18), 3789–3798.

Zhang, Y., Li, X., Wang, Z., & Chen, Q. (2024). Advanced thermal modeling of submerged PV modules under varying hydrological conditions. *Journal of Renewable and Sustainable Energy*, ***16***(1), 013502.

Zhou, Y., & Poon, A. W. (2023). Temperature-modulated Rayleigh scattering. *IEEE Photonics Journal*, ***15***(2).

Zhou, Y., Zhang, H., & Xu, W. (2021). Hydrodynamic-optical coupling in natural waters. *Limnology and Oceanography*, ***66***(3), 891–905.

Zhou, Y., Wang, L., Chen, H., & Li, X. (2022). Water-column attenuation physics for submerged photovoltaic systems. *Optics Express*, ***30***(12), 20458–20472.